

1 **A long-term high-resolution air quality reanalysis with public facing air quality dashboard**
2 **over the Contiguous United States (CONUS)**

3

4 Rajesh Kumar¹, Piyush Bhardwaj^{1,*}, Cenlin He¹, Jennifer Boehnert¹, Forrest Lacey¹, Stefano
5 Alessandrini¹, Kevin Sampson¹, Matthew Casali¹, Scott Swerdlin¹, Olga Wilhelmi¹, Gabriele G.
6 Pfister¹, Benjamin Gaubert¹, and Helen Worden¹

7

8 ¹NSF National Center for Atmospheric Research, Boulder, CO, USA

9 *Now at Center for Study of Science, Technology and Policy (CSTEP), Bengaluru, India

10

11 Corresponding author: Rajesh Kumar (rkumar@ucar.edu)

12

13 Keywords: Chemical data assimilation, WRF-CMAQ, GSI, Air Quality Dashboard

14

15

16

17 **Abstract**

18 We present a 14-year 12-km hourly air quality dataset created by assimilating satellite observations
19 of aerosol optical depth (AOD) and carbon monoxide (CO) in an air quality model to fill gaps in
20 the contiguous United States (CONUS) air quality monitoring network and help air quality
21 managers understand long-term changes in county level air quality. Specifically, we assimilate the
22 Moderate Resolution Imaging Spectroradiometer (MODIS) AOD and the Measurement of
23 Pollution in the Troposphere (MOPITT) CO observations in the Community Multiscale Air
24 Quality Model (CMAQ) every day from 01 Jan 2005 to 31 Dec 2018 to produce this dataset. The
25 Weather Research and Forecasting (WRF) model simulated meteorological fields are used to drive
26 CMAQ offline and to generate meteorology dependent anthropogenic emissions. Both the weather
27 and air quality (surface fine particulate matter (PM_{2.5}) and ozone) simulations are subjected to a
28 comprehensive evaluation against multi-platform observations to establish the credibility of our
29 dataset and characterize its uncertainties. We show that our dataset captures regional hourly,
30 seasonal, and interannual variability in meteorology very well across the CONUS. The correlation
31 coefficient between the observed and simulated surface ozone and PM_{2.5} concentrations for
32 different Environmental Protection Agency (EPA) defined regions across CONUS are 0.77-0.91
33 and 0.49-0.79, respectively. The mean bias and root mean squared error for modeled ozone are
34 3.7-6.8 ppbv and 7-9 ppbv, respectively, while the corresponding values for PM_{2.5} are -0.9-5.6
35 $\mu\text{g}/\text{m}^3$ and 3.0-8.3 $\mu\text{g}/\text{m}^3$, respectively. We estimate that annual CONUS averaged maximum daily
36 8-hour average (MDA8) ozone and PM_{2.5} trends are -0.30 ppb/year and -0.24 $\mu\text{g}/\text{m}^3/\text{year}$,
37 respectively. Wintertime MDA8 ozone shows an increasing but statistically insignificant trend at
38 several sites. We also found a decreasing trend in the 95th percentile of MDA8 ozone but an
39 increasing trend in the 5th percentile. Most of the sites in the Pacific Northwest show an increasing

40 but statistically insignificant trend during summer. An ArcGIS air quality dashboard has been
41 developed to enable easy visualization and interpretation of county level air quality measures and
42 trends by stakeholders, and a Python-based Streamlit application has been developed to allow the
43 download of the air quality data in simplified text and graphic formats.

44

45

46 1. Introduction

47 Air quality is one of the most important global environmental concerns as almost the entire global
48 population (99%) is estimated to breathe air that exceeds the World Health Organization (WHO)
49 defined Air Quality Guidelines (WHO, 2023). Exposure to ambient air pollution causes about 4.2
50 million premature mortalities every year (WHO, 2020). Air quality has improved substantially
51 over the past two decades in the US as the Environmental Protection Agency (EPA) observations
52 show that maximum daily 8h average (MDA8) surface ozone levels have decreased by 29% over
53 1980-2021, and annual average concentrations of particulate matter with an aerodynamic diameter
54 smaller than 2.5 μm ($\text{PM}_{2.5}$) have decreased by 37% over 2000-2021 ([https://www.epa.gov/air-](https://www.epa.gov/air-trends/air-quality-national-summary)
55 [trends/air-quality-national-summary](https://www.epa.gov/air-trends/air-quality-national-summary)). However, air pollution continues to violate the National
56 Ambient Air Quality Standards (NAAQS) in many parts of the US, such as the Colorado Front
57 Range, California, northeast US, and nearly all the national parks. A recent study reported that
58 97% of US national parks suffer from significant or unsatisfactory levels of harm from air pollution
59 (Orozco et al., 2024). Poor air quality is reported to cause about 160,000 premature deaths in the
60 US, with a total economic loss of about \$175 billion (Im et al., 2018). Exposure to air pollution
61 levels even below the EPA NAAQS can adversely affect human health (Di et al., 2017). To
62 mitigate the risks of air pollution and how air quality is responding to emission control policies, it
63 is, therefore, imperative to quantify past changes in air quality.

64 Numerous studies have revealed several key features of long-term changes in surface ozone
65 and $\text{PM}_{2.5}$ over the US using long-term observations from the EPA monitoring networks. First,
66 both the urban and rural sites in the eastern US show negative ozone trends during the summer
67 season (Butler et al., 2011; Cooper et al., 2012), but lower ozone levels at some sites have an
68 increasing trend during winter and early spring (Bloomer et al., 2010; Cooper et al., 2012; Simon

69 et al., 2015). Second, surface and free tropospheric ozone show positive trends in all seasons at
70 rural and remote sites in the western US (Jaffe and Ray, 2007; Cooper et al., 2012). Third,
71 increasing ozone is observed in the inflow to the US west coast (Jaffe et al., 2003), over the North
72 Pacific (Parrish et al., 2004), and west coast marine boundary layer (Parrish et al., 2009). The
73 Tropospheric Ozone Assessment Report (TOAR) showed that summertime surface ozone
74 continues to decrease over the US, but the trend is less certain at the urban sites (Chang et al.,
75 2017; Fleming et al., 2018). Similar regional and seasonal differences in the long-term trends are
76 also seen in PM_{2.5} and its components. For example, carbonaceous aerosols (organic and black
77 carbon) show a widespread decrease over 1990-2010 across the US in winter and spring and show
78 positive but insignificant trends over the western US (Hand et al., 2013). PM_{2.5} levels continue to
79 decrease over the majority of the US except in the wildfire-prone areas (McClure and Jaffe, 2018).

80 In addition to the observation-based trend analysis, chemical transport model (CTM)
81 simulations have been employed to interpret the observed trends. For example, the increase in
82 lower ozone values can be attributed to the increase in Asian emissions from 1980-1995 (Fiore et
83 al., 2002). The anthropogenic emissions and natural variability were found to have competing
84 effects on surface ozone over much of the US over 1980-2005 (Pozzoli et al., 2011). Another study
85 reproduced negative summertime ozone trends over the eastern US but underestimated the positive
86 trends in the western US likely due to underestimation of Asian emission trends or trans-pacific
87 transport or changes in stratosphere-troposphere exchange (Koumoutsaris and Bey, 2012). Lin et
88 al. (2017) quantified the contributions of rising Asian emissions, domestic U.S. emission controls,
89 wildfires and climate to changes in surface ozone from 1980 to 2014. Several studies have also
90 quantified the contributions of wildfires to PM_{2.5} trends in the U.S. (Xie et al., 2020, Burke et al.,
91 2023). While global models captured most of the observed variability and trends in summertime

92 ozone, the use of high-resolution regional models is recommended to reproduce interannual
93 variability in winter and spring in the western US (Strode et al., 2015).

94 Apart from the interpretation of observed trends, the CTMs also provide information in
95 areas with no observations. However, CTM simulations suffer from both systematic (i.e., biases)
96 and random errors due to a number of factors, including numerical approximations, inadequate
97 understanding of some processes that control the spatial and temporal distribution of air pollutants,
98 inaccuracies in the initialization of the physical and chemical atmospheric state, and uncertainties
99 in the emission inventories. While continuous efforts are being made to improve the representation
100 of processes controlling PM_{2.5} and ozone (Appel et al., 2010, 2013, 2017; Nolte et al., 2015; Fahey
101 et al., 2017) and emission inventories are updated by the EPA every three years, recent
102 developments have shown that assimilation of the National Aeronautics and Space Administration
103 (NASA) satellite retrievals of atmospheric composition in CTMs can significantly improve air
104 quality simulations (Gaubert et al., 2016; Kumar et al., 2019; Liu et al., 2011; Pagowski et al.,
105 2014; Saide et al., 2013). NASA satellite retrievals of atmospheric constituents with a far greater
106 spatial coverage compared to ground-based monitoring networks presents a unique opportunity to
107 develop long-term high-resolution air quality reanalysis, which can be useful for quantifying air
108 quality changes in unmonitored areas and assessing the impacts of changes in air quality on human
109 health and ecosystems.

110 This paper describes the methodology and evaluation of a long-term high-resolution
111 regional air quality reanalysis generated over the CONUS from 2005 to 2018 by assimilating the
112 Moderate Resolution Imaging Spectroradiometer (MODIS) aerosol optical depth (AOD) and the
113 Measurement of Pollution in the Troposphere (MOPITT) carbon monoxide (CO) retrievals daily
114 in the Community Multiscale Air Quality (CMAQ) model. Our regional reanalysis is based on

115 three-dimensional variational (3DVAR) approach, which is different compared to the four-
116 dimensional variational (4D-Var) approach (Innes et al., 2019) and Ensemble Kalman Filter
117 approaches (Gaubert et al. 2017, Miyazaki et al., 2020, Kong et al., 2021) used in recent long-term
118 global and regional air quality reanalysis. Among these, 3DVAR is computationally the most
119 efficient approach because it uses only a single model simulation, but its accuracy can be limited
120 by the assumption of a constant background error covariance matrix that both 4DVAR and EnKF
121 address. An air quality dashboard developed to enable the use of this dataset by a variety of
122 stakeholders is also described.

123

124 **2. Methodology**

125 **2.1. The Chemical Transport Model**

126 The CMAQ model version 5.3.2 driven offline by the Weather Research and Forecasting (WRF)
127 model version 4.1 is used to simulate air quality over the CONUS from 01 Jan 2005 to 31 Dec
128 2018. We employ the “cb6r3_ae7_aq” chemical mechanism that uses Carbon Bond 6 version r3
129 for gas-phase chemistry and AERO7 aerosol module for representing aerosol processes, including
130 secondary organic aerosols (Appel et al., 2021). Both the WRF and CMAQ models use a horizontal
131 grid spacing of 12 x 12 km² with WRF (CMAQ) grid using 481 (442), 369 (265), 36 (35) grid
132 points in the longitudinal, latitudinal, and vertical directions, respectively. The model top is set to
133 50 hPa for both the models. The meteorological initial and boundary conditions for WRF are based
134 on the six hourly ERA-Interim analyses at a grid spacing of 0.7° x 0.7°. We follow Appel et al.
135 (2017) for physical parameterizations, four-dimensional data assimilation, and soil moisture
136 nudging settings in WRF.

137 Emissions from several anthropogenic emissions sectors such as residential wood combustion,
138 agricultural emissions from livestock and fertilizer applications, and mobile sources depend on
139 meteorological conditions. For example, ambient temperature affects the heating demand, affects
140 the volatilization of emissions from fertilizer use, drives air conditioning use, etc. The SMOKE
141 modeling system allows us to simulate these relationships. To be consistent in the use of
142 meteorological fields for both emission processing and driving CMAQ, we generate meteorology-
143 dependent anthropogenic emissions for the EPA National Emissions Inventory (NEI) base years
144 of 2011, 2014, and 2017 by feeding the WRF meteorological fields to the Sparse Matrix Operator
145 Kernel Emissions (SMOKE). The emissions for 2005-2010 are derived by applying EPA reported
146 annual state-wise trends to the NEIv2 2011 emissions. While NEI emissions are available for 2005
147 and 2008, the emissions processing platform for 2005 and 2008 does not process emissions for the
148 “cb6r3_ae7_aq” chemical mechanism of CMAQ used here. Similarly, NEIv2 2014 emissions are
149 used to derive emissions for 2012 and 2013, and the NEIv1 2017 emissions are used to derive
150 anthropogenic emissions for the rest of the years. Fire emissions in CMAQ are represented using
151 the Fire Inventory from NCAR (FINN) version 2.2 which provides daily varying global fire
152 emissions at 1 x 1 km² resolution (Wiedinmyer et al., 2023). FINN emissions are processed through
153 SMOKE to enable inline plume rise of fire emissions within CMAQ. Biogenic emissions are
154 calculated online within the model using the Biogenic Emission Inventory System (BEIS). The
155 chemical boundary conditions are based on 6-hourly Whole Atmosphere Community Climate
156 Model (WACCM) simulations (Marsh et al., 2013; Gettelman et al., 2019). The WACCM output
157 is mapped onto CMAQ grids using the Initial Conditions Processor (ICON) and Boundary
158 Conditions Processor (BCON).
159

160 2.2. Data Assimilation System

161 We have used the three-dimensional variational (3DVAR) capability of the community Gridpoint
162 Statistical Interpolation (GSI) version 3.5 to assimilate the Level 2 MODIS AOD retrievals and
163 the Level 2 MOPITT CO retrievals in CMAQ. The MODIS AOD assimilation framework is the
164 same as we developed previously (Kumar et al., 2019) and the MOPITT CO assimilation capability
165 has been developed in this work. We use total aerosol mass per mode (Aiken, Accumulation, and
166 Coarse) and CO mixing ratios as the control variables in GSI. The state variables include individual
167 aerosol components, total aerosol mass per mode, CO mixing ratios, meteorological variables
168 (temperature, pressure, and relative humidity), and CMAQ vertical grid. Daily MODIS and
169 MOPITT retrievals are converted into a format compatible with GSI input modules.

170 A climatological background error covariance (BEC) matrix is generated separately for
171 winter (January) and summer (July) conditions using the GEN_BE tool, which reads two different
172 WRF-CMAQ runs driven by different meteorological and emission inputs but valid at the satellite
173 overpass time. Since there are multiple overpasses of the Terra and Aqua satellites that host the
174 MOPITT and MODIS sensors, we calculate the BEC at 15 Z, 18 Z, and 21 Z. The winter BEC is
175 used when assimilating satellite retrievals from November through March and the summer BEC is
176 used for the rest of the months. Our BEC design considers the uncertainties in meteorology,
177 anthropogenic, and biomass burning emissions. Meteorological uncertainties are represented by
178 using two different sets of physical parameterizations (Table A3.1) in two WRF runs to capture
179 errors in meteorology related to assumptions used in physical parameterizations. Species-
180 dependent perturbation factors for anthropogenic and biomass burning emissions are estimated by
181 comparing a number of available global/regional anthropogenic and biomass burning emission
182 inventories over the CONUS (Table A3.2 and A3.3). Among the two WRF-CMAQ runs fed to

183 GEN_BE for BEC estimation, we used the default emissions in the first run and perturbed the
184 emissions in the second run. The BEC was then estimated in terms of variances and length scales
185 (both horizontal and vertical) for total aerosol mass per mode and CO, and used in GSI. We refer
186 the reader to Kumar et al. (2019) for a description of BEC parameters.

187 We have assimilated standard Level 2 Collection 6.1 MODIS AOD and Version 8
188 MOPITT CO retrievals based on the multispectral algorithm (thermal and near infrared) in CMAQ.
189 This multispectral product is more sensitive to near-surface CO over land compared to the thermal-
190 infrared only retrievals. MOPITT retrievals agree with in-situ measurements at all vertical levels
191 within $\pm 5\%$ (Deeter et al., 2019). The observation errors for MODIS AOD retrievals are specified
192 as $(0.03 + 0.05 * \text{AOD})$ and $(0.05 + 0.15 * \text{AOD})$ over the ocean and the land, respectively (Remer
193 et al., 2005). The observation errors for CO profiles are used as reported in the MOPITT retrieval
194 product. A simple forward operator and its adjoint based on the parameterization of (Malm and
195 Hand, 2007) is used to convert CMAQ aerosol chemical composition into AOD for a direct
196 comparison with MODIS AOD retrievals as described in Kumar et al. (2019). The forward
197 operator and its adjoint for MOPITT CO assimilation are developed in this study and described in
198 Appendix A1.

199

200 **2.3. Reanalysis production workflow**

201 Daily analyses of three-dimensional fields of aerosols and CO based on the assimilation of MODIS
202 AOD and MOPITT CO retrievals in CMAQ using the GSI system has been performed using the
203 workflow shown in Figure 1. The first CMAQ simulation on 01 Jan 2005 is initialized using the
204 global model simulations from WACCM, and all subsequent simulations until 31 Dec 2018 are
205 initialized from the previous CMAQ simulations. Every day, we perform 9 simulations following

206 the availability of new satellite observations every three hours owing to difference between Terra
207 and Aqua overpass times. The first simulation runs CMAQ from 00-15 Z, the second simulation
208 assimilates MODIS Terra and Aqua AOD retrievals at 15 Z, and third simulation assimilates
209 MOPITT CO retrievals at 15 Z. The fourth simulation advances CMAQ from 15 Z to 18 Z with
210 the fifth and sixth simulations assimilating MODIS AOD and MOPITT CO at 18Z, respectively.
211 The seventh simulation advances CMAQ from 18 Z to 21 Z, the eighth simulation assimilates
212 MODIS Aqua AOD retrievals at 21 Z, and the ninth simulation advances CMAQ from 21 Z to 00
213 Z of the next day. This resulted in a total of 46,152 jobs submission on the NCAR supercomputer
214 Cheyenne (https://arc.ucar.edu/knowledge_base/70549542). An automated script was developed
215 to submit and track successful completion of these jobs.

216 The assimilation times of 15 Z, 18 Z, and 21 Z were determined based on the analysis of
217 overpass times of Terra and Aqua satellites, which pass over the CONUS between 13:30 Z and
218 22:30 Z. All the satellite retrievals belonging to a 3-hour window are assumed to be available for
219 assimilation at the center of that window. For example, all the satellite retrievals between 1330 Z
220 and 1630 Z are assimilated at 1500 Z.

221 Our previous work has shown that the assimilation of MODIS AOD in CMAQ improved
222 the correlation coefficient between CMAQ simulated and independently observed PM_{2.5} by ~67%
223 and reduced the mean bias by ~38% over the CONUS during July 2014. To understand whether
224 GSI pushes CMAQ towards MOPITT, we performed and compared one month (July 2018) of
225 CMAQ experiments with and without assimilation of MOPITT CO profiles. We find that the
226 assimilation of MOPITT CO profiles substantially improves the correlation coefficient and reduces
227 the errors (both mean bias and root mean squared error) between CMAQ and MOPITT CO at all
228 the pressure levels except at 100 hPa where the MOPITT sensitivity is the lowest (Appendix A2,

229 Figure A2.1). This simple test confirms the ability of GSI to constrain the performance of CMAQ
230 with satellite observations. Other trace gas species (e.g., ozone and OH) are not affected directly
231 by the assimilation of AOD and CO, but the impact of assimilation indirectly affects these species
232 through photochemical processes in the model. For example, we found instantaneous changes in
233 surface ozone in the range of -1.3 to 3.2 ppbv but monthly average changes are within the range
234 of ± 0.3 ppbv during July 2018.

235

236 **2.4. Output frequency and optimization**

237 The production of a chemical reanalysis also poses a challenge of storing the model output. Since
238 our chemical reanalysis focuses on air quality applications, we saved all the chemical variables
239 together with relevant meteorological parameters (2 m temperature and relative humidity, 10 m
240 wind speed and direction, planetary boundary layer height, precipitation, and downward reaching
241 solar radiation) and deposition (both dry and wet) fluxes every hour at the surface. The total size
242 of this output is 12 Terabytes.

243

244 **3. Ground-based observations and trend calculation method**

245 We have obtained and processed hourly in-situ measurements of 2 m temperature (T2), 2 m relative
246 humidity (RH), 10 m wind speed (WS10), 10 m wind direction (WD10), and surface pressure from
247 the METeorological Aerodrome Reports (METAR) network, which is distributed by the NCEP's
248 Meteorological Assimilation Data Ingest System (MADIS). METAR data are surface weather
249 observations and it consists of meteorological data from airports (Automated Surface Observing
250 Systems) and other permanent weather stations (Automated Weather Observing System) located
251 throughout the US. We used the Level-3 Quality Controlled METRAR data over CONUS to

252 evaluate our modeled meteorological fields (https://madis.ncep.noaa.gov/madis_metar.shtml).
253 Daily precipitation data from the 0.1-deg Integrated Multi-satellitE Retrievals for Global
254 precipitation measurements (IMERG; <https://gpm.nasa.gov/data/imerg>) dataset is used to evaluate
255 WRF simulated precipitation.

256 To evaluate the modeled surface PM_{2.5} and ozone concentrations, we have obtained hourly
257 PM_{2.5} and ozone observations from the EPA Air Quality System, which currently measures PM_{2.5}
258 and ozone at more than 1000 sites across the US. The AQS data also contains values below the
259 method detection limit (MDL). The MDLs are different for ozone and PM_{2.5} and also vary as a
260 function of site and instrument type. For consistency, we assume the MDL values of 5 ppb for
261 ozone and 2 µg/m³ for PM_{2.5} for all sites. All the data below MDL was replaced by MDL/2
262 (<https://www3.epa.gov/ttnamti1/files/ambient/airtox/workbook/AirtoxWkbk4Preparingdataforan>
263 [analysis.pdf](https://www3.epa.gov/ttnamti1/files/ambient/airtox/workbook/AirtoxWkbk4Preparingdataforan); <https://pubs.acs.org/doi/10.1021/es071301c>). The sites for which two simultaneous
264 measurements (corresponding to two instruments) were available, the mean value is taken for
265 further calculation.

266 The trend calculations were performed using both the observed and modeled ozone and
267 PM_{2.5} values. The monthly mean time series of observed and modeled maximum daily 8-hour
268 (MDA8) ozone and 24-hour average PM_{2.5} during 2005-2018 is calculated over all measurement
269 sites. The daily MDA8 ozone over a site is calculated using the EPA's defined methodology
270 (<https://www.govinfo.gov/content/pkg/FR-2015-10-26/pdf/2015-26594.pdf>, pp 168). For each
271 day, 8-hour running averages are taken from 7 am to 11 pm local standard time, which constitutes
272 17 8-hour running mean values per day. If an 8-hour window has less than 6 hours of data and the
273 mean value of the remaining hours is less than 70 ppb then the data for that window is discarded.
274 If a site has fewer than 13 valid 8-hour mean values or the maximum value of the available 8-hour

275 average is less than 70 ppb then the value for that day is discarded. For PM_{2.5}, a daily 24-hour
276 average value is calculated in local standard time only if at least 18 hours of valid data/day are
277 available. Furthermore, we discarded all sites with (1) < 50% data per month, (2) < 50 % data
278 during each year, and (3) if number of years with $\geq 50\%$ data were < 10 years during 2005-2018.
279 The number of valid sites fulfilling the above criteria over CONUS are estimated to be 1012 and
280 369, for MDA8 ozone and 24-hour PM_{2.5}, respectively. Daily values of MDA8 ozone and 24-hour
281 PM_{2.5} are used to calculate monthly 5th percentile, 50th percentile, 95th percentile and mean time
282 series during 2005-18 at each valid site. A similar criterion for seasonal mean, 5th, 50th and 95th
283 percentile time series was also used. The number of valid sites during summer season were the
284 maximum (1010/357 for MDA8 O₃/24-hour PM_{2.5}) and were minimum (501/337 for MDA8
285 O₃/24-hour PM_{2.5}) during the winter season. These annual and seasonal MDA8 ozone and PM_{2.5}
286 time series are then used to estimate annual and seasonal trends and the significance of trend values
287 are also tested.

288

289 **4. Results and Discussions**

290 **4.1. Meteorological evaluation**

291 The WRF simulations for the entire period (2005-2018) processed using the Meteorology-
292 Chemistry Interface Processor (MCIP) are collocated with METAR observations of T2, RH,
293 WS10, and WD10 in space and time, and paired values are used for evaluating the model. The
294 evaluation is performed at a regional scale following the EPA regional classification of the
295 CONUS in 10 regions (see Appendix A2, Figure A2.2). The number of METAR sites during 2005-
296 2018 was 1290, and the maximum available hourly data during the study period was 33-68 % over
297 10 EPA regions. Region 8 has the least data (~33-37%), and other regions have 47-68 % data

298 during 2005-2018. Monthly regional averaged model and METAR observations time series are
299 compared over 10 EPA regions for T2 (Figure 2), RH (Figure 3), WS10 (Figure 4), and WD10
300 (Figure 5). Three statistical metrics, namely correlation coefficient (r), mean bias (MB), and root
301 mean square error (RMSE), for each region are also listed in Figures 2-5.

302 Monthly regional averaged T2 between model and observations (Figure 2) show excellent
303 correlations of 0.8-1.0 with low mean biases of -0.3 to 0.4 °C and the RMSE ranging from 2.0-5.7
304 °C over the 10 EPA regions. The model also performed well ($r = 0.7-0.9$) in simulating RH (Figure
305 3) over 10 EPA regions with the mean biases of 0.9-3.6 % and the RMSE of 12.5 - 16.3 %. Since
306 RH is estimated as a ratio of vapor pressure to saturation pressure (e_s) and e_s depends on T2, the
307 biases in T2 also contribute to the biases in RH. For example, EPA Region 6 which shows the
308 highest T2 RMSE also shows the highest RH RMSE. The model reproduces the variations in
309 surface pressure very well ($r = 1.0$) with a slight underestimation (MB = -8.1 to 0.2 hPa; RMSE =
310 0.3-8.1 hPa). The slight underestimation in pressure is seen in eight out of 10 EPA regions with
311 the largest MB in Regions 9 (-8.1 hPa) and 10 (-7.4 hPa). The errors in surface pressure (plot not
312 shown) over these regions could also contribute to biases in T2 and RH.

313 Prior to 10 m wind speed comparison, model wind speeds are assigned “zero value” if the
314 hourly wind speed at any site is less than 0.51 m/s (1 knot). This step was needed to make model
315 output consistent with the METAR wind speed data, which treats such wind speeds as calm winds
316 and assigns it a zero value. Our model simulation slightly overestimates (MB = 0.1-0.8 m/s) WS10
317 (Figure 4) over most of EPA regions with the exception of Region 8 (MB = -0.1 m/s). Wind
318 direction (Figure 5) biases (absolute) over these regions were 34°-58°. The correlation coefficients
319 for both WS10 and WD10 are slightly lower in Regions 8-10, which is likely due to the complex
320 topography in these regions. The correlation coefficients for 10 m wind speed were lower than

321 those for temperature, and relative humidity, indicating a slightly poorer model performance for
322 winds. The WRF model is known to overpredict 10 m wind speed at low to moderate wind speeds
323 in all available planetary boundary layer (PBL) schemes (Mass and Ovens, 2010). This
324 shortcoming of the model was partly attributed to unresolved topographical features by the default
325 surface drag parameterization, which in turn influences surface drag and friction velocity, and
326 partly to the use of coarse horizontal and vertical resolutions of the domain (Cheng et al., 2005).
327 The WRF model also captures the seasonally averaged diurnal variations in T2, RH, and 10 m
328 Wind speed very well but overestimates the wind speed particularly at night (see Appendix A2,
329 Figure A2.3).

330 Since WRF and IMERG precipitation have different resolutions, we first mapped the WRF
331 simulated precipitation from a 12 km x 12 km grid on Lambert conformal projection to the IMERG
332 rectilinear grid of 0.1° x 0.1° using the “rcm2rgrid” functionality of the NCAR command language
333 (<https://www.ncl.ucar.edu/Document/Functions/Built-in/rcm2rgrid.shtml>). The seasonal mean
334 WRF simulated and IMERG derived precipitation are then compared over four seasons during
335 2005-2018 (Figure 6). The model is able to capture the spatial patterns in precipitation in different
336 seasons, with an underestimation of -0.1 to -0.9 mm/day. The highest underestimation is observed
337 during the winter season. The eastern CONUS showed an underestimation during winter, spring
338 and autumn seasons, however, over the western US, the model mostly overestimated the
339 precipitation, especially in the mountainous regions (Rockies, Cascades, and Sierra Nevada). The
340 model also showed larger biases over the lakes and oceanic regions. Despite the biases, this
341 comprehensive evaluation shows that our model simulations captured the key features of regional
342 and temporal variability of the key meteorological parameters over the CONUS fairly well.

343

344 4.2. Air Quality evaluation

345 Hourly regional averaged observed and CMAQ simulated surface ozone and PM_{2.5} are
346 compared for all the EPA regions in Figures 7 and 8, respectively. In all the regions, the model
347 captures the seasonal cycle in surface ozone characterized by a summertime peak as well as the
348 observed interannual variability very well, with correlation coefficients of 0.77 to 0.91. The model
349 also overestimates the nighttime ozone levels in all the regions (see Appendix A2, Figure A2.4),
350 but a larger overestimation is seen in Regions 8 and 9. The mean bias and RMSE in modeled ozone
351 are very similar across the regions, with values ranging from 3.7 - 6.8 ppbv and 7.0-9.0 ppbv,
352 respectively. The model shows a slightly poorer skill in capturing the variability in PM_{2.5} relative
353 to ozone as reflected by smaller r values of 0.49-0.79 but captures long-term trends in most of the
354 regions reasonably well. The mean bias and RMSE in modeled PM_{2.5} are estimated to be -0.9 to
355 5.6 µg/m³ and 3.0 to 8.3 µg/m³, respectively. The largest underestimation of PM_{2.5} is seen in
356 Region 8, particularly from 2005 to 2012 while the largest overestimation is seen in Region 2.

357 In addition to regional evaluation, we also evaluated the model performance for different
358 land use types and location settings (see Appendix A2, Figure A2.5 for classification of the number
359 of sites in these categories). This categorization information by land use and location types was
360 not available for a very small number of sites, and thus, they were excluded from the analysis (sites
361 classified as “NONE” in Figure A2.2). Since Maximum Daily Averaged 8-hour (MDA8) ozone
362 and daily averaged PM_{2.5} are policy-relevant metrics, we focus on the evaluation of these
363 parameters on a monthly averaged scale for this evaluation. We evaluate monthly median (50th
364 percentile), 5th and 95th percentile time series of MDA8 ozone, and daily averaged PM_{2.5} for
365 different land use categories and location settings (Appendix A2, Figures A2.6-A2.11).

366 Among the rural sites, all land use categories showed the highest biases for the 5th
367 percentile, followed by the median and 95th percentile for MDA8 ozone, except for the “Others”
368 category, for which the median showed the lowest bias. For suburban and urban site types, 95th
369 percentile MDA8 ozone consistently showed the lowest bias for all land use types, followed by
370 the median and 5th percentile. Furthermore, “Others” land use category under the rural and urban
371 sites shows the lowest bias for 5th percentile and the median, while “residential” land use type
372 shows the lowest bias for the suburban sites.

373 For PM_{2.5}, the largest differences between the model and observations are seen for the 95th
374 percentile at “Others” land use categories compared to the 5th percentile and median. The model
375 generally captures the temporal variability in PM_{2.5} across all land use types (except “Others”) and
376 location settings for all three-percentile metrics analyzed here but some anomalies are also evident.
377 For example, residential and commercial sites in the urban category show larger overestimation
378 for the median and 95th percentiles during 2005-2006, indicating higher uncertainties in
379 anthropogenic emission estimates at these sites during these years. While the model follows most
380 of the observed peaks in 95th percentile, it substantially underestimates the observed peaks.

381 The errors in air quality simulations can be attributed to the uncertainties in different types
382 of emissions used to drive air quality models, errors in the lateral boundary conditions representing
383 pollution inflow, uncertainties in meteorological parameters (as quantified earlier in this section),
384 and poor understanding of some of the physical and chemical processes controlling the fate of
385 those emissions. To quantify uncertainties in anthropogenic and biomass burning emissions over
386 the CONUS, we compared all available anthropogenic and biomass burning emission inventories
387 over the CONUS and found that anthropogenic emission estimates across various emission
388 inventories vary by a factor of 1.16 - 2.94 (Table A3.2) and the corresponding fire emission

389 estimates vary by 3.13 - 8.0 (Table A3.3). The extrapolation of the NEI emissions to years other
390 than the base years might have also introduced some uncertainties in our simulations because EPA
391 reported state level trends may not always represent local (sub-state) changes in emissions and
392 also do not provide information about new emission sources appearing in the CONUS between
393 two NEI base emission inventory years. In addition, the observation error ($0.05 + 15\%$ of MODIS
394 AOD value over land; Remer et al., 2005) for MODIS AOD increases with increase in the
395 magnitude AOD which in turn restricts the data assimilation system (GSI) in pushing the modeled
396 AOD towards the MODIS AOD. Furthermore, the AOD retrievals do not contain any information
397 about the vertical distribution of aerosols and thus GSI simply scales the modeled vertical profile
398 to match the MODIS AOD within the constraints of observation and model error. Thus, AOD
399 assimilation is unable to correct for any errors in vertical distribution of aerosols resulting from
400 errors in the plume rise of fire emissions.

401

402 **4.3. Trend analysis**

403 To help air quality managers and the public determine the confidence they can put in using this
404 reanalysis for analyzing changes in air quality in their regions, we have evaluated the trends in our
405 CMAQ simulated MDA8 ozone and 24-hr average $PM_{2.5}$ against the AQS observations. The
406 spatial distribution of positive/negative trend values in MDA8 ozone and 24-hr average $PM_{2.5}$
407 calculated using monthly median values in AQS and CMAQ data during 2005-2018 are shown in
408 Figures 9 and 10, respectively. Different symbols are used to represent urban, suburban, and rural
409 site types. Based on location, $\sim 42/23\%$ of sites were in rural areas, $\sim 41/45\%$ in suburban areas
410 and $\sim 17/32\%$ were in urban or city centers, respectively, for MDA8 ozone/24-hr average $PM_{2.5}$.
411 Darker/lighter red and blue colors represent statistically significant/insignificant increasing and

412 decreasing trends at 2-sigma level. The 2-sigma rule is a standard way of testing statistical
413 significance of trends. In a normal distribution, ~95% of the data points lie within 2 standard
414 deviations (± 2 -sigma) of the mean. If the trend falls outside this range, it is considered unlikely to
415 have occurred by chance (i.e., at a statistical significance in the probability of less than 5%). Over
416 the study period, both the model and observations show decreasing trends in MDA8 ozone over
417 the majority of the CONUS. Most eastern US sites show decreasing trends that were statistically
418 significant with p values less than 0.05. The sites located in western/northwestern US, however,
419 showed mixed results with some sites showing increasing trends, most of which were not
420 statistically significant. Similar results were observed during the summer season with most sites
421 showing statistically significant decreasing trends over the most locations. During autumn and
422 winter seasons, several sites over California and the eastern US showed decreasing but
423 insignificant trends. Some sites over the midwestern US also changed the trend sign during these
424 seasons. The trends in winter seasons were mostly positive over most sites in the US (except for
425 the coastal sites in the southeastern US). About 55% (278 of 501) of the sites showed positive
426 trends in both AQS and CMAQ data during winter but only ~3% (29 of 1012) of the sites showed
427 positive trends in summer. The seasonal changes in monthly median trends discussed above were
428 mostly consistent (67-86%) between the AQS and CMAQ data. A similar analysis with 5th and
429 95th percentile time series suggested that the higher percentiles showed mostly decreasing trends,
430 but 5th percentile dataset at the mid-western US, Boston-New York-DC, and central US sites
431 showed increasing trends on a seasonal and annual basis. The MDA8 ozone trend over CONUS
432 (1012 sites) is estimated to be $-0.53 \pm 0.46/-0.56 \pm 0.45$ ppb/year (summertime) and $-0.31 \pm 0.43/-$
433 0.29 ± 0.39 ppb/year (annual), respectively, for AQS/CMAQ data, with most sites (~70 %)
434 showing negative trends. At the 2-sigma level (p-value < 0.05), the summertime mean ozone trends

435 are $-0.85 \pm 0.36 / -0.75 \pm 0.35$ ppb/year for 484/620 sites and annual MDA8 ozone trends are -0.52
436 $\pm 0.45 / -0.47 \pm 0.42$ ppb/year for 554/562 sites, respectively, for AQS/CMAQ data over CONUS.
437 This suggests decreases in monthly high ozone days but increases in monthly low ozone. On an
438 annual basis, MDA8 ozone showed the most decreasing trends (AQS/CMAQ = $-0.40 \pm 0.37 / -0.34$
439 ± 0.34 ppb/year) in the 428 rural sites. The mean ozone trends over urban (411 sites) and suburban
440 (170) areas were (AQS/CMAQ = $-0.28 \pm 0.44 / -0.29 \pm 0.40$ ppb/year) and (AQS/CMAQ = $-0.13 \pm$
441 $0.48 / -0.15 \pm 0.48$ ppb/year), respectively. The ozone trends over high-altitude sites (16 sites), are
442 mostly negative for AQS/CMAQ = $-0.43 \pm 0.45 / -0.12 \pm 0.36$ ppb/year) in summer and annually
443 (AQS/CMAQ, = $-0.39 \pm 0.38 / -0.03 \pm 0.29$ ppb/year).

444 Similar MDA8 ozone trends were also reported in a previous study (Simon et al., 2015).
445 Mousavinezhad et al. (2023) reported that all regions except the Northern Rockies and the
446 Southwest experienced decreasing trends in median MDA8 ozone values during the warm season
447 of 1991-2020, with rural stations in the Southeast and urban stations in the Northeast experiencing
448 the greatest declines of -1.29 ± 0.07 ppb/year and -0.85 ± 0.08 ppb/year, respectively. They also
449 reported a large decrease in MDA8 ozone 95th percentile in all regions. Similarities in ozone trends
450 between the AQS observations and CMAQ simulations over a longer time period 1990-2015 is
451 also reported by He et al. (2020).

452 On an annual basis, 24-hr average $PM_{2.5}$ also showed mostly decreasing trends ($\sim 79\%$)
453 over most of the sites. A majority of these trends were also statistically significant at 2-sigma level
454 (AQS/CMAQ = $70\% / 75\%$). However, unlike MDA8 ozone, an increasing trend (though
455 insignificant) in summertime $PM_{2.5}$ is observed over the north-western US (Fig. 10). The
456 wintertime trends were also mostly decreasing over most of the sites, except for the northwestern
457 US. During summer season about 5-fold increase (annual $\sim 5\%$; summer $\sim 24\%$) in positive trends

458 is observed in high PM_{2.5} days (95th percentile time series) and most of these increases were
459 observed over the Pacific Northwest. These summertime increases in PM_{2.5} trends are also evident
460 from the 95th percentile time series, where a sharp increase in PM_{2.5} is observed during 2017-2018
461 overall sites except industrial locations (see Figure A2.11). In recent years these changes could be
462 even stronger as wildfire activity over the western US has increased in the last decade. The
463 dramatic decreasing trends of PM_{2.5} in the eastern US were also reported in previous studies
464 (Zhang et al., 2018; Gan et al., 2015; Xing et al., 2015) (Gan et al., 2015; Xing et al., 2015; Zhang
465 et al., 2018) due to emission reductions. The increasing trend in the western central area is due in
466 part to frequent wildfires (Dennison et al., 2014; McClure and Jaffe, 2018). For PM_{2.5} the overall
467 mean trends are $-0.24 \pm 0.21/-0.24 \pm 0.24$ $\mu\text{g}/\text{m}^3/\text{year}$ (369 sites) in AQS/CMAQ data sets. Unlike,
468 MDA8 ozone, the number of sites remained almost the same (337-357 sites in four seasons, 369
469 annual) during seasons and an overall negative trend is also observed (-0.18 ± 0.25 to -0.30 ± 0.35
470 $\mu\text{g}/\text{m}^3/\text{year}$). At 2-sigma level, the number of sites that showed negative trends in both the datasets
471 were 69-80 %.

472 On an annual basis, the mean PM_{2.5} trends over urban sites are $-0.17 \pm 0.22/-0.18 \pm 0.15$
473 $\mu\text{g}/\text{m}^3/\text{year}$, suburban sites are $-0.28 \pm 0.22/-0.24 \pm 0.26$ $\mu\text{g}/\text{m}^3/\text{year}$ and -0.3 $\mu\text{g}/\text{m}^3/\text{year}$, and urban
474 and city center are $-0.23 \pm 0.21/-0.30 \pm 0.27$ $\mu\text{g}/\text{m}^3/\text{year}$ $\mu\text{g}/\text{m}^3/\text{year}$, respectively, for AQS/CMAQ
475 data. The only high-altitude site for PM_{2.5} showed an increase in the annual ($0.07/0.06$ $\mu\text{g}/\text{m}^3/\text{year}$
476 for AQS/CMAQ data) and summertime trend ($0.13/0.13$ $\mu\text{g}/\text{m}^3/\text{year}$ for AQS/CAMQ data).
477 During other seasons, mostly low negative trends were observed. The ozone trends over high-
478 altitude sites (16 sites), however, are mostly negative ($-0.43 \pm 0.45/-0.12 \pm 0.36$ ppb/year in
479 summer and $-0.39 \pm 0.38/-0.03 \pm 0.29$ ppb/year, annually). The ozone trends at high altitude sites

480 showed large seasonal variations with min to max ranges of -0.69 to 0.87/-1.5 to 0.26 ppb/year for
481 AQS/CMAQ data.

482

483 **4.4. Air Quality dashboard**

484 The comprehensive evaluation of our reanalysis in the above sections shows that our
485 reanalysis is able to capture key features of long-term trends in both MDA8 ozone and PM_{2.5} over
486 most parts of the CONUS. This increases confidence in using this dataset for assessing the trends
487 in unmonitored areas of the CONUS. Therefore, a Geographic Information System (GIS)-based
488 dashboard has been developed to aid in community engagement and understanding of the
489 reanalysis data. The dashboard was developed using Esri ArcGIS Dashboard technology (Esri,
490 2024). An interactive web-based dashboard allows stakeholders to explore air quality annual
491 concentrations and the number of days that exceed a certain threshold over space and time. It
492 provides a step-by-step path for users to explore information at the CONUS, state, and county
493 levels. In the center of the dashboard is a time series chart showing trends in annual concentrations
494 of MDA8 ozone, NO₂, PM_{2.5}, PM₁, and PM₁₀ between 2005 and 2018. An indicator element of a
495 dashboard highlights how many days between 2005 and 2018 have exceeded the National Ambient
496 Air Quality Standards (NAAQS) for ozone and PM_{2.5}, and a bar chart graph shows the number of
497 days that exceeded the NAAQS each year. There is also a map that zooms to the selected state or
498 county of interest and illustrates the spatial distribution of air quality variables using a quantitative
499 color bar.

500 The dashboard can be used to better understand how particular events, such as large
501 wildfires, have affected air quality in certain geographic areas. For example, the 2008 wildfires in
502 Shasta and Trinity Counties in California, referred to as the June Fire Siege, had a major impact

503 on air quality (<https://storymaps.arcgis.com/stories/c6535ee477e14b72a20393a5f10aefbc>). Figure
504 11 shows MDA8 ozone concentrations for Shasta County, California. The dashboard shows a
505 sharp increase in MDA8 ozone concentration in 2008, as depicted in the time series plot. The bar
506 chart in the lower right corner also reflects the large number of days that exceeded the NAAQS
507 criteria for MDA8 ozone in 2008.

508 The dashboards also can be used to visualize the efficacy of air quality management
509 policies. For example, Los Angeles County, CA has designed and implemented strict emission
510 standards to improve air quality. Figure 12 shows the downward trend in PM_{2.5} concentrations in
511 Los Angeles County during 2005-2018. The air quality dashboard is publicly accessible at
512 <https://ncar.maps.arcgis.com/apps/dashboards/9a97650dc77b4f7192b99ea9bef36a21>. To ensure
513 stakeholders have an understanding of the uncertainties, we have included the following message
514 on the website: “Note that mean bias of 3.7-6.8 ppbv in ozone and that of -0.9-5.6 µg/m³ in PM_{2.5}
515 could have impacted the calculation of days exceeding the corresponding National Ambient Air
516 Quality Standards.”

517 We have also developed a Python-based Streamlit application allowing users to select and
518 download data for specific time periods aggregated over administrative boundaries such as cities,
519 counties, and states. Temporal and spatial aggregations are performed on the server, and only
520 information of interest is downloaded and delivered to the users, taking the data processing
521 workload off of the users. The Streamlit application allows users to select a time period, a temporal
522 aggregation (daily, weekly, monthly, annual), one or more air quality variables, statistics (min,
523 mean, max), and an area of interest (state, county, city). The data can then be downloaded as a
524 comma-separated file as well as graphed on the website as seen in Figure 13. The Streamlit
525 application is available at: <https://compass.rap.ucar.edu/airquality/>

526

527 **5. Data availability**

528 The global meteorological datasets used to drive WRF are publicly available through National
529 Center for Atmospheric Research (NCAR) Research Data Archive (<https://rda.ucar.edu/>). The
530 SMOKE setup used to create emissions for CMAQ is accessible via EPA emissions modeling
531 platform (<https://www.epa.gov/air-emissions-modeling/emissions-modeling-platforms>). FINN
532 biomass burning emissions can be downloaded from <https://rda.ucar.edu/datasets/ds312.9/>.
533 Meteorological observations used to evaluate the model performance are downloaded from
534 <https://madis-data.cprk.ncep.noaa.gov/madisPublic1/data/archive/>. The EPA AQS system
535 observations are downloaded from <https://www.epa.gov/aqs>. Hourly surface output from the
536 WRF-CMAQ-GSI system can be downloaded from <https://doi.org/10.5065/cfya-4g50> (Kumar and
537 He, 2023)

538

539 **6. Code availability**

540 The WRF, CMAQ, and GSI source codes are publicly accessible at <https://github.com/wrf-model/>,
541 <https://github.com/USEPA/CMAQ>, and [https://dtcenter.org/community-code/gridpoint-](https://dtcenter.org/community-code/gridpoint-statistical-interpolation-gsi/download)
542 [statistical-interpolation-gsi/download](https://dtcenter.org/community-code/gridpoint-statistical-interpolation-gsi/download).

543

544 **7. Conclusions**

545 Air pollution is an important health hazard affecting human health and the economy in the
546 CONUS, yet millions of people live in counties without air quality monitors. To address this gap
547 and help air quality managers understand long-term changes in air qualities at the county level
548 across the CONUS, we have created a 14-year long 12-km hourly dataset by daily assimilation of

549 atmospheric composition observations from the NASA MODIS and MOPITT sensors aboard the
550 Terra and Aqua satellites in the Community Multiscale Air Quality (CMAQ) model from 01 Jan
551 2005 to 31 Dec 2018. The WRF model has been used to simulate meteorological parameters,
552 which are then used to drive CMAQ offline and for generating meteorology-dependent
553 anthropogenic emissions.

554 The meteorological parameters, ozone, and PM_{2.5} have been extensively validated against
555 multi-platform observations to characterize uncertainties in our dataset, which air quality managers
556 need to determine the confidence they can put in our dataset. We show that our dataset captures
557 regional scale hourly, seasonal, and interannual variability in the meteorological variability well
558 across the CONUS. The model shows an excellent performance in simulating the regional and
559 temporal variability in temperature and relative humidity but a slightly poorer performance in
560 simulating winds and precipitation, which are well known shortcomings of the WRF model. The
561 model also shows a higher skill in reproducing variabilities in surface ozone ($r = 0.77-0.91$) than
562 PM_{2.5} ($0.49-0.79$). The mean biases for CMAQ ozone and PM_{2.5} are estimated to be 3.7-6.8 ppbv
563 and -0.9-5.6 $\mu\text{g}/\text{m}^3$, respectively, and the corresponding RMSE values are 7-9 ppbv and 3.0-8.3
564 $\mu\text{g}/\text{m}^3$, respectively.

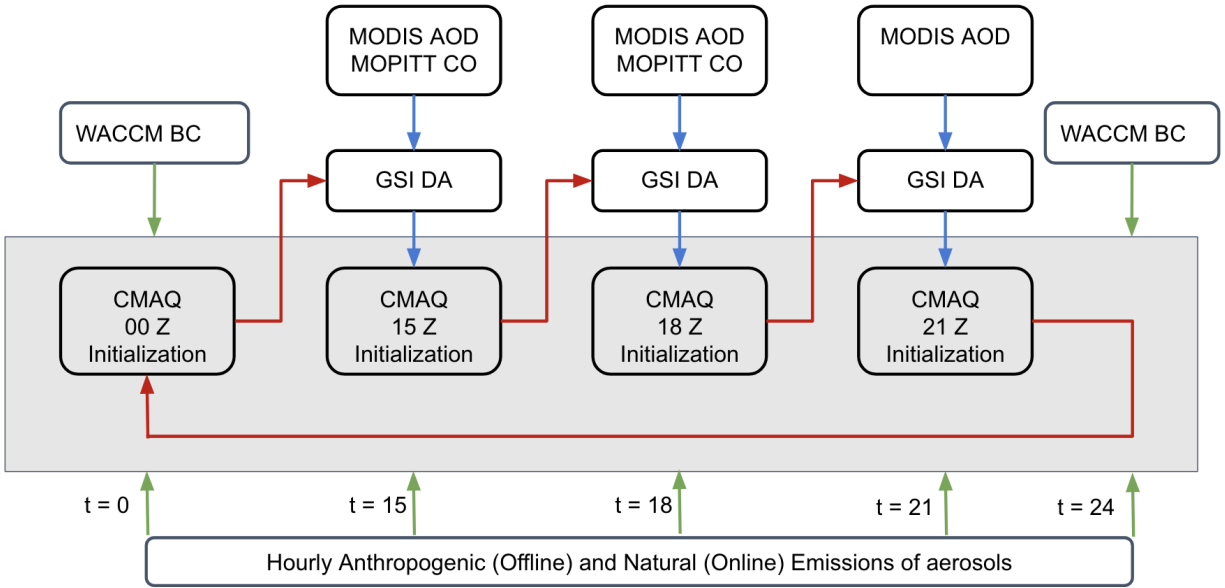
565 The MDA8 ozone trend over CONUS is estimated to be $-0.53 \pm 0.46/-0.56 \pm 0.45$ ppb/year
566 (summertime) and $-0.31 \pm 0.43/-0.29 \pm 0.39$ ppb/year (annual), respectively, for AQS/CMAQ data
567 with ~70% of sites showing negative trends. At a 2-sigma level, the summertime MDA8 ozone
568 trends are $-0.85 \pm 0.36/-0.75 \pm 0.35$ ppb/year and annual MDA8 ozone trends are $-0.52 \pm 0.45/-$
569 0.47 ± 0.42 ppb/year, respectively, for AQS/CMAQ data over CONUS. Annually, at 2-sigma level,
570 46% sites showed negative trends in both the data. Annual mean PM_{2.5} trends are $-0.24 \pm 0.21/-$
571 0.24 ± 0.24 $\mu\text{g}/\text{m}^3/\text{year}$, respectively in AQS/CMAQ data sets, and ~79% of the sites showed

572 negative trends. Annually, at 2-sigma level, 66% sites showed negative trends in both the data.
573 During summertime, the negative trend percent is reduced to 71%, where an increase in positive
574 trends are observed in the northwestern US.

575 An air quality dashboard has been developed, which provides a step-by-step path for users
576 to explore information at the CONUS, state, and county levels. This dashboard allows the users to
577 visualize air quality information in the form of maps, bar charts, and the NAAQS exceedance days.
578 Finally, a Python-based Streamlit application is developed to allow the download of the air quality
579 data in simplified text and graphic formats for the end user's choice of the region and time of
580 interest.

581

582 8. Figures



583

584 **Figure 1:** Architecture of the daily GSI/CMAQ based chemical data assimilation workflow.

585

586

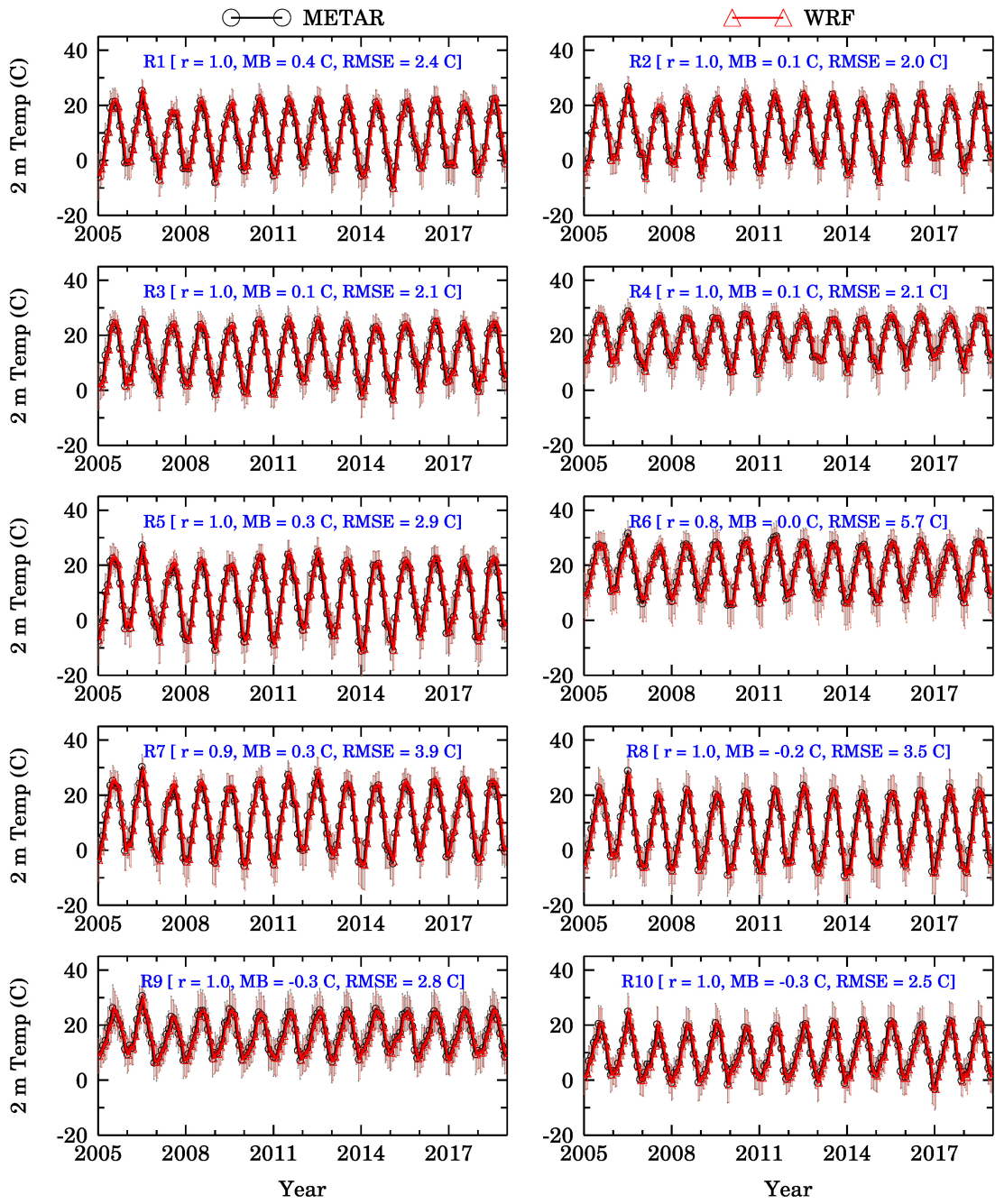
587

588

589

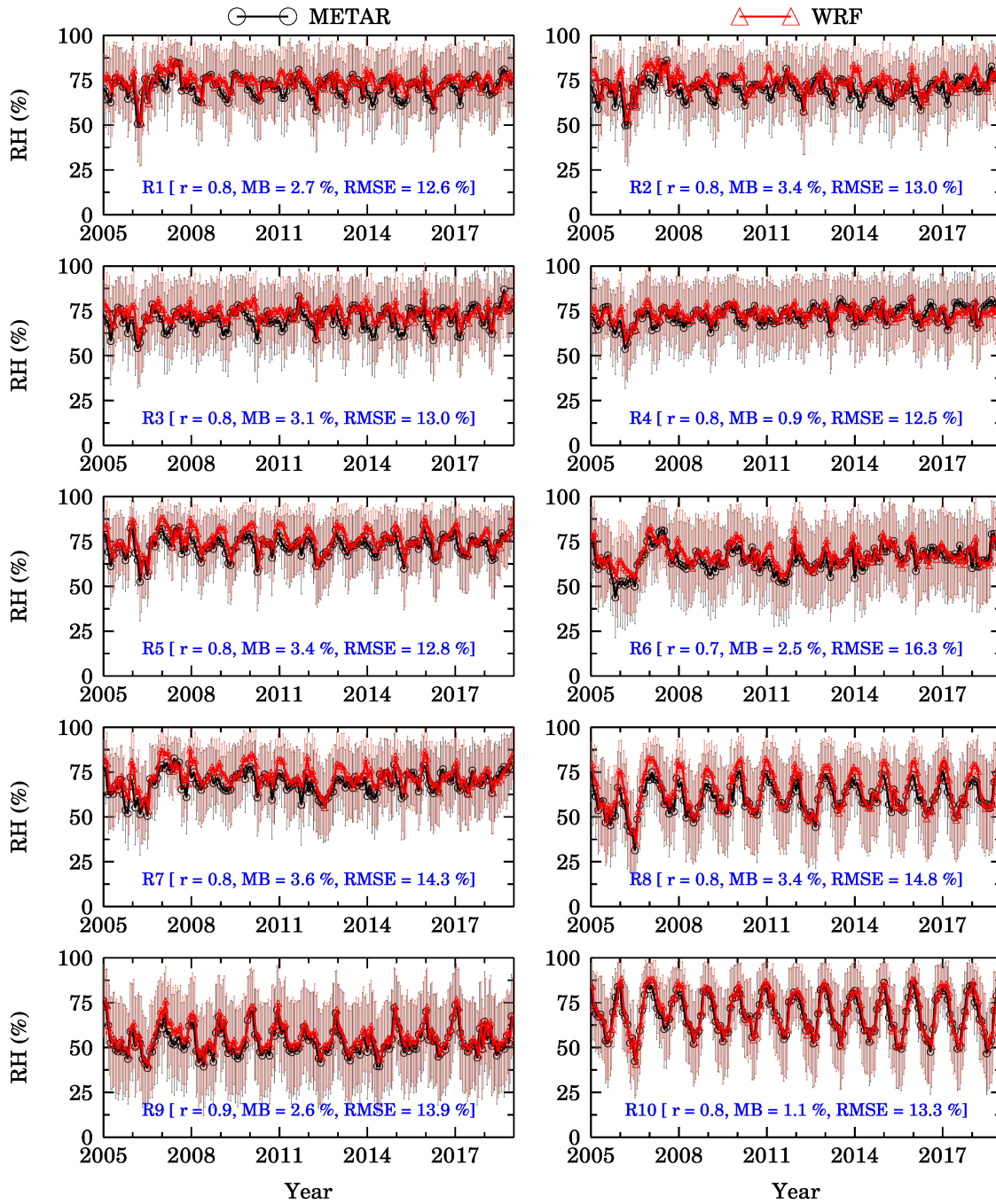
590

591



592

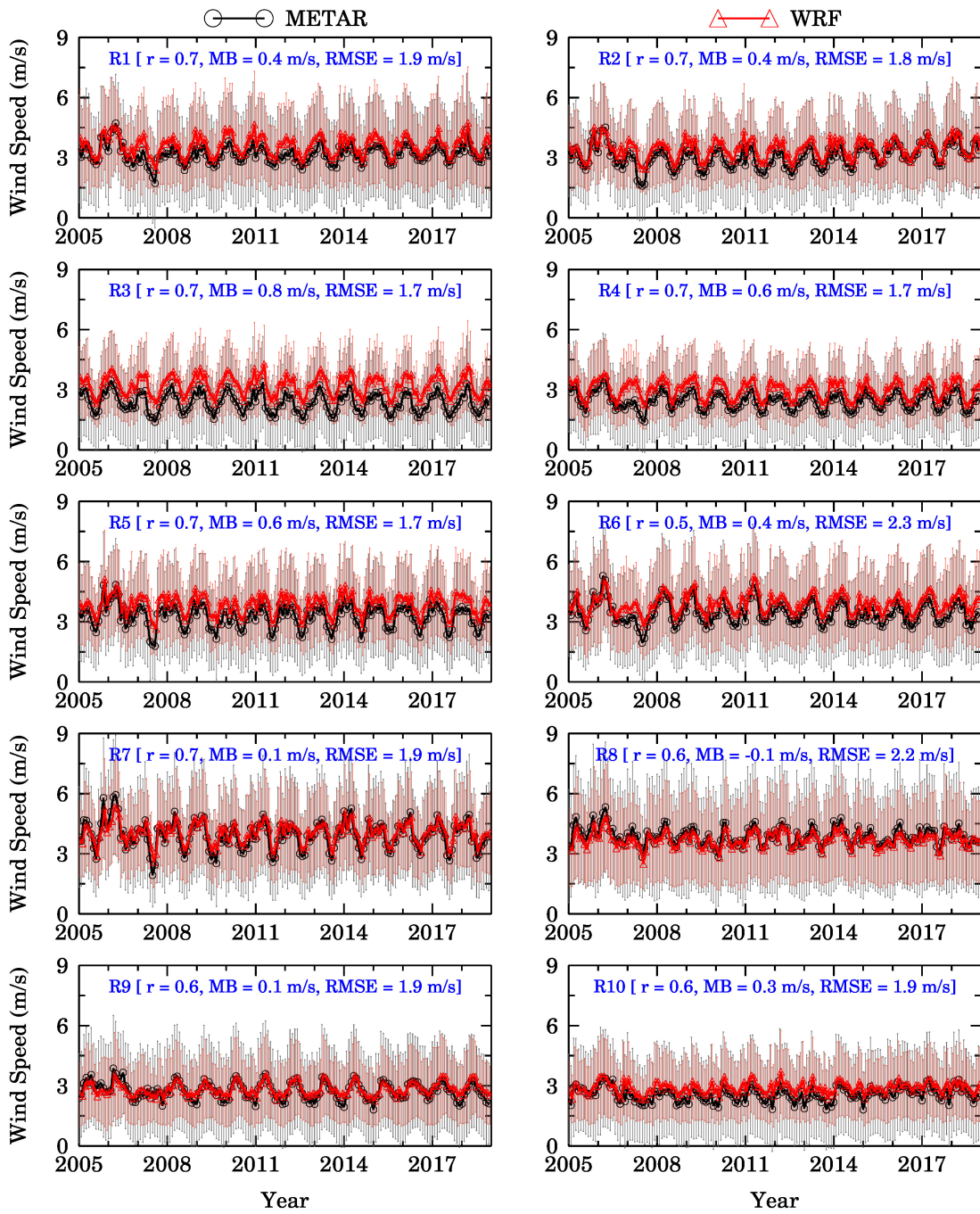
593 **Figure 2:** Time series of monthly averaged 2 m temperature over 10 EPA regions (R1-R10) from
 594 WRF-CMAQ setup (red) and METAR observations (black) during 2005-2018. Orange and Grey
 595 lines represent the standard deviation for WRF-CMAQ and METAR, respectively. The correlation
 596 coefficient (r), mean bias (MB), and the root mean square error (RMSE) for each region is also
 597 shown.



598

599 **Figure 3:** Same as Figure 2 but for 2 m relative humidity (RH).

600

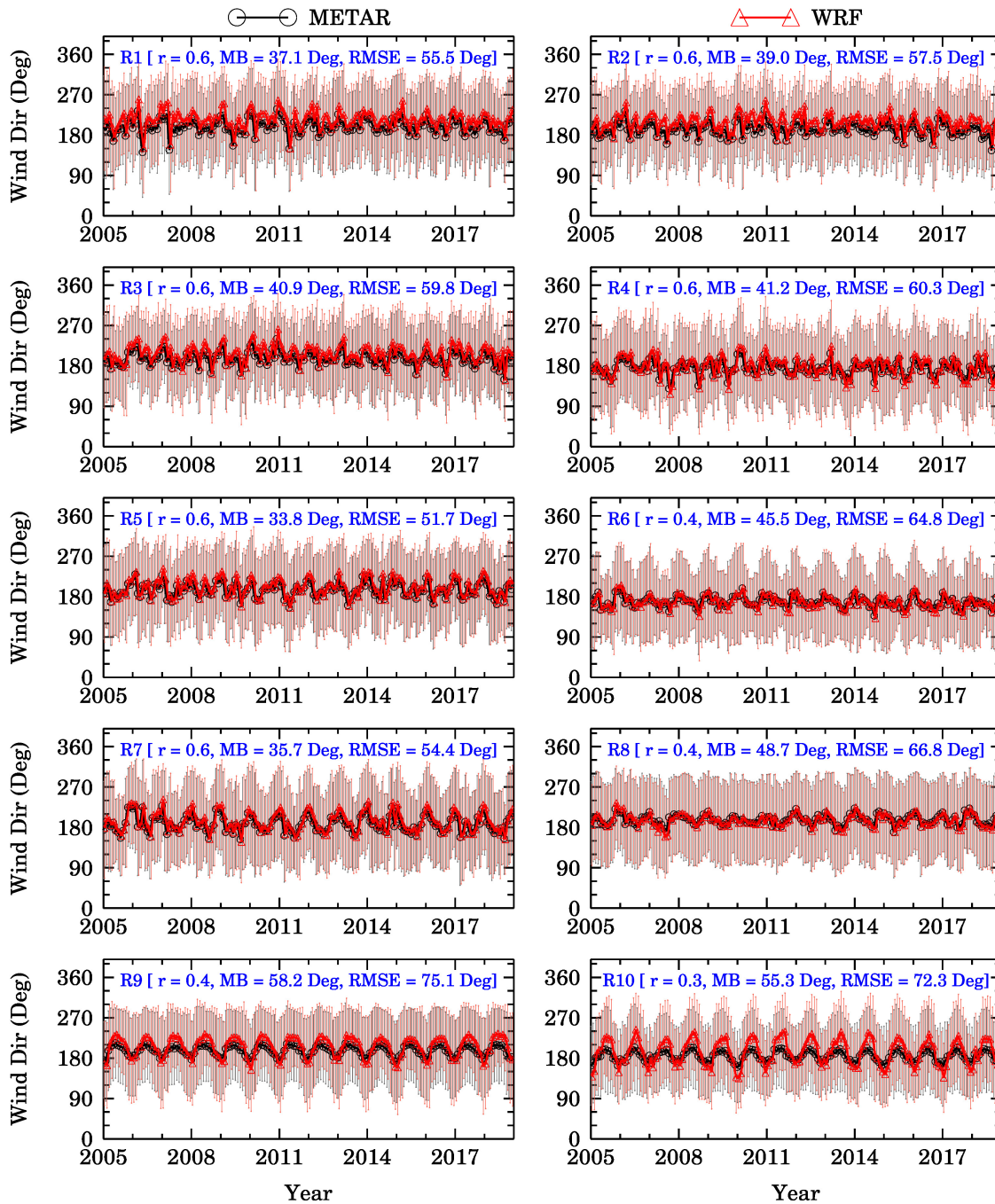


601

602 **Figure 4:** Same as Figure 2 but for 10 m wind speed.

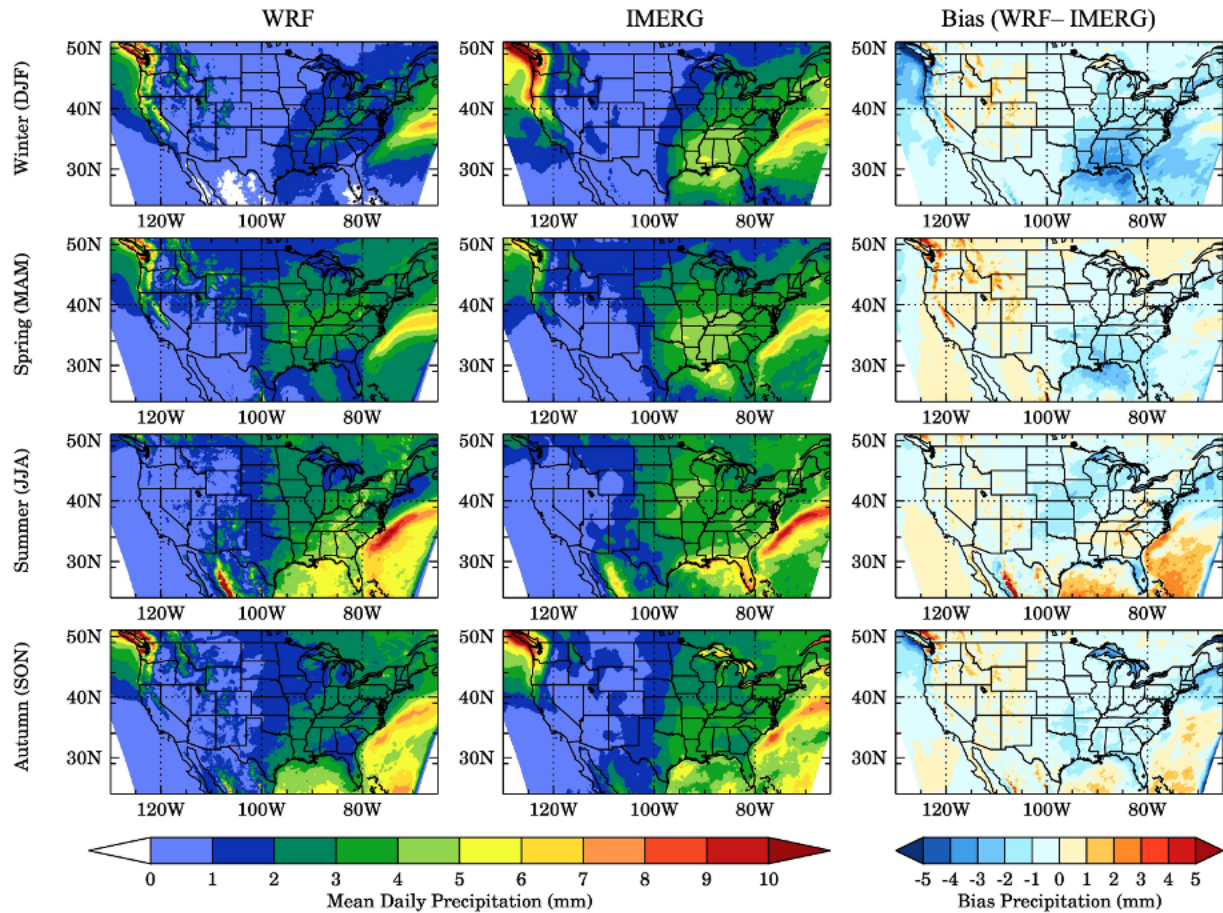
603

604



605

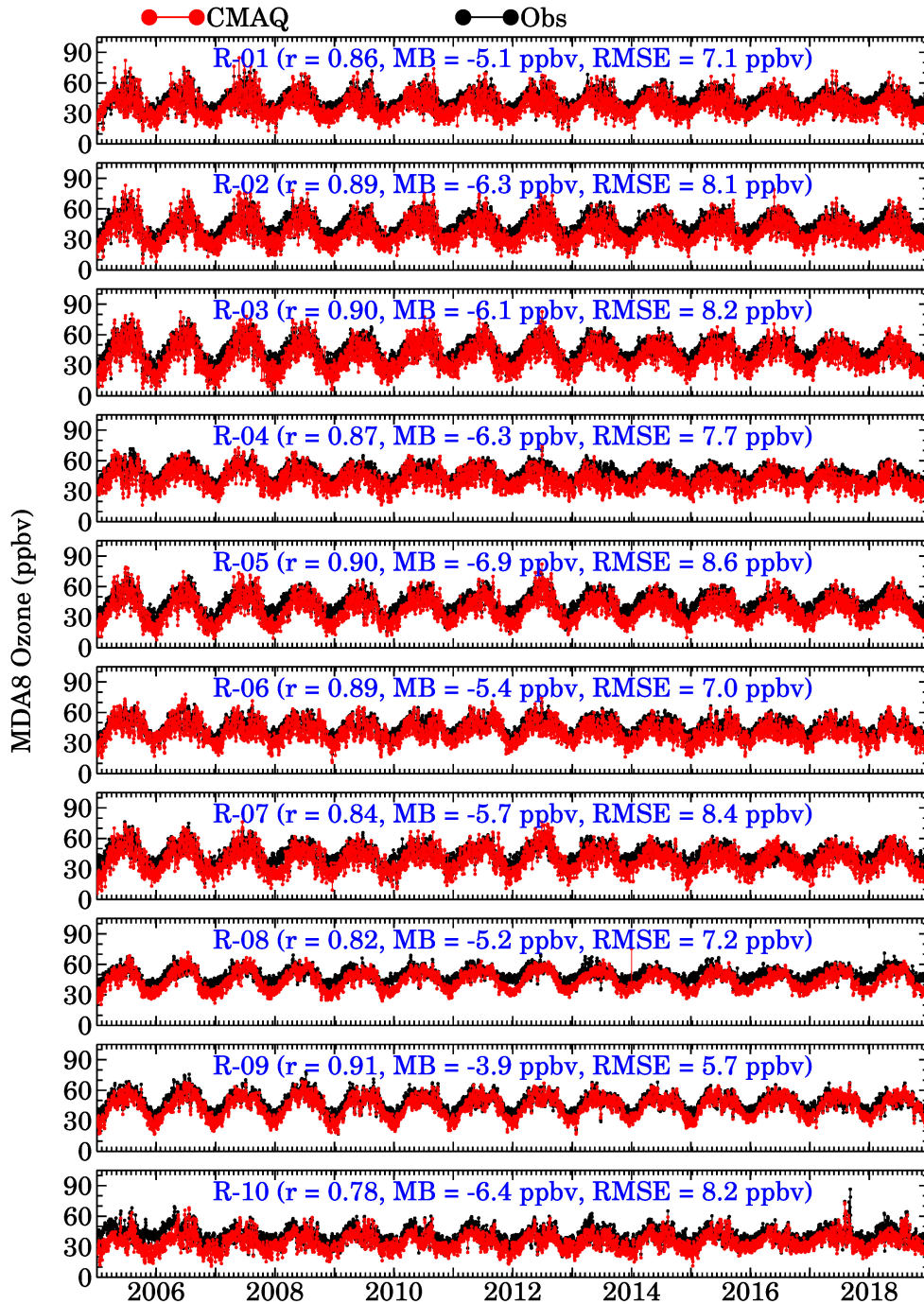
606 **Figure 5:** Same as Figure 2 but for 10 m wind direction.



607

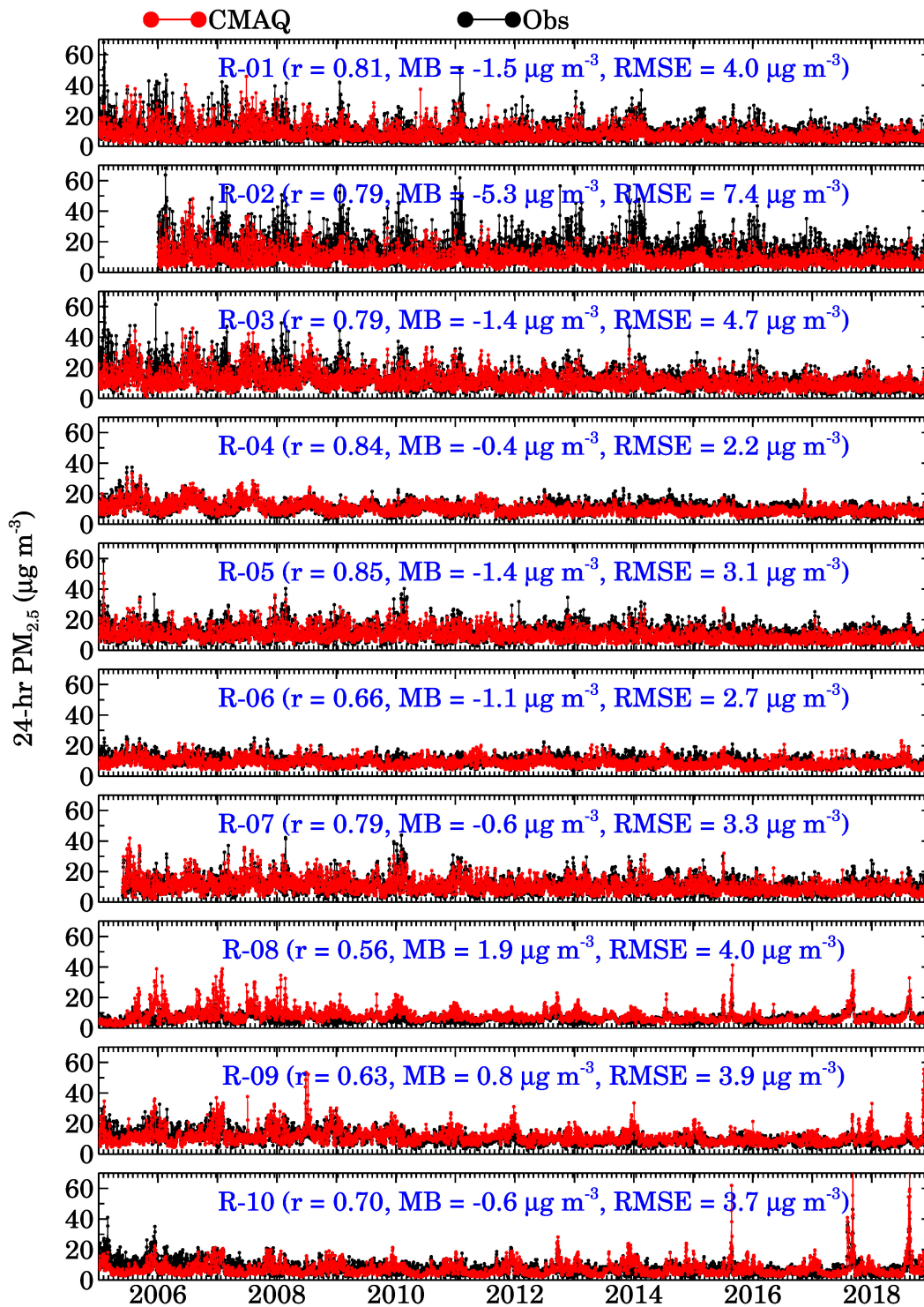
608 **Figure 6:** Spatial distribution of mean daily precipitation and bias during four seasons in 2005-
 609 2018 (top to bottom, *viz.*, Winter, Spring, Summer and Autumn). Left, center and right panels
 610 represent mean precipitation from WRF, IMERG and bias (WRF-IMERG) precipitation,
 611 respectively.

612



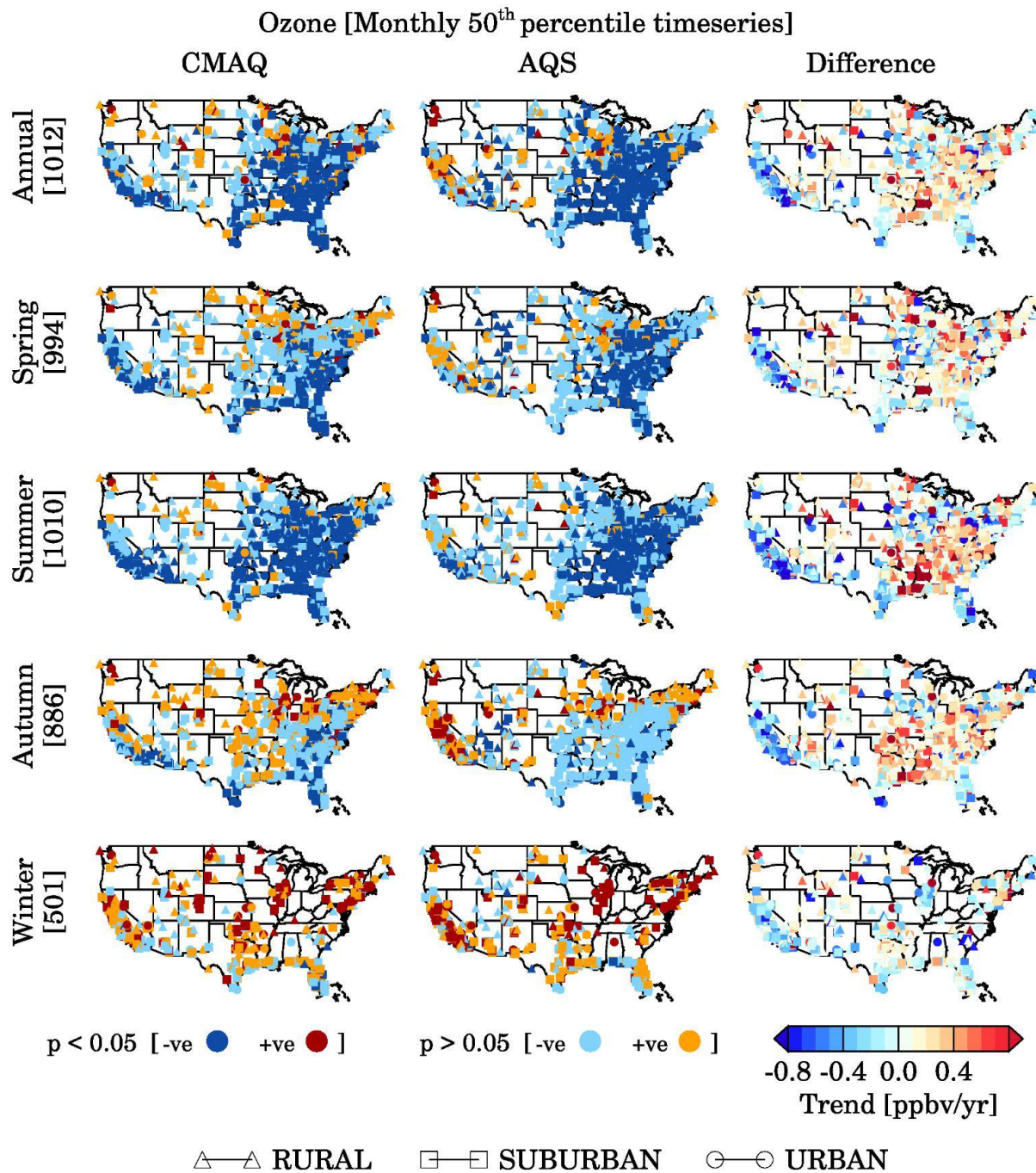
613

614 **Figure 7:** Time series of hourly averaged surface ozone over 10 EPA regions (R1-R10) from
 615 WRF-CMAQ setup (red) and EPA AQS observations (black) during 2005-2018. The correlation
 616 coefficient (r), mean bias (MB), and the root mean square error (RMSE) for each region is also
 617 shown.



619

620 **Figure 8:** Same as Figure 7 but for daily averaged surface fine particulate matter ($PM_{2.5}$).

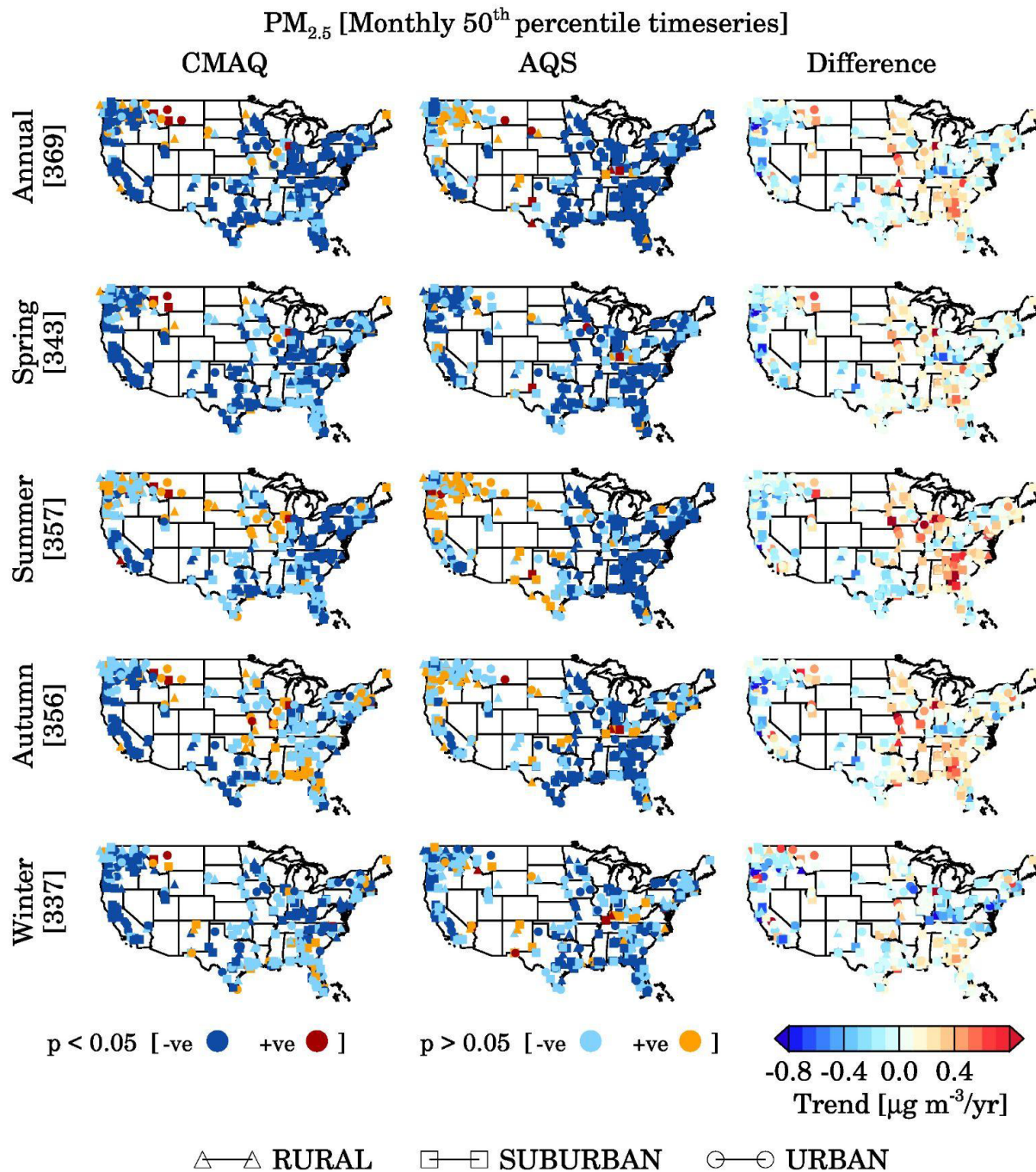


621

622 **Figure 9:** Spatial distribution of positive (blue colors), negative trends (red colors) in MDA8 ozone

623 at different statistically significant levels (p-values) using annual, seasonal monthly median time

624 series (top to bottom). Plots on the right show differences in trend values [CMAQ-AQS].



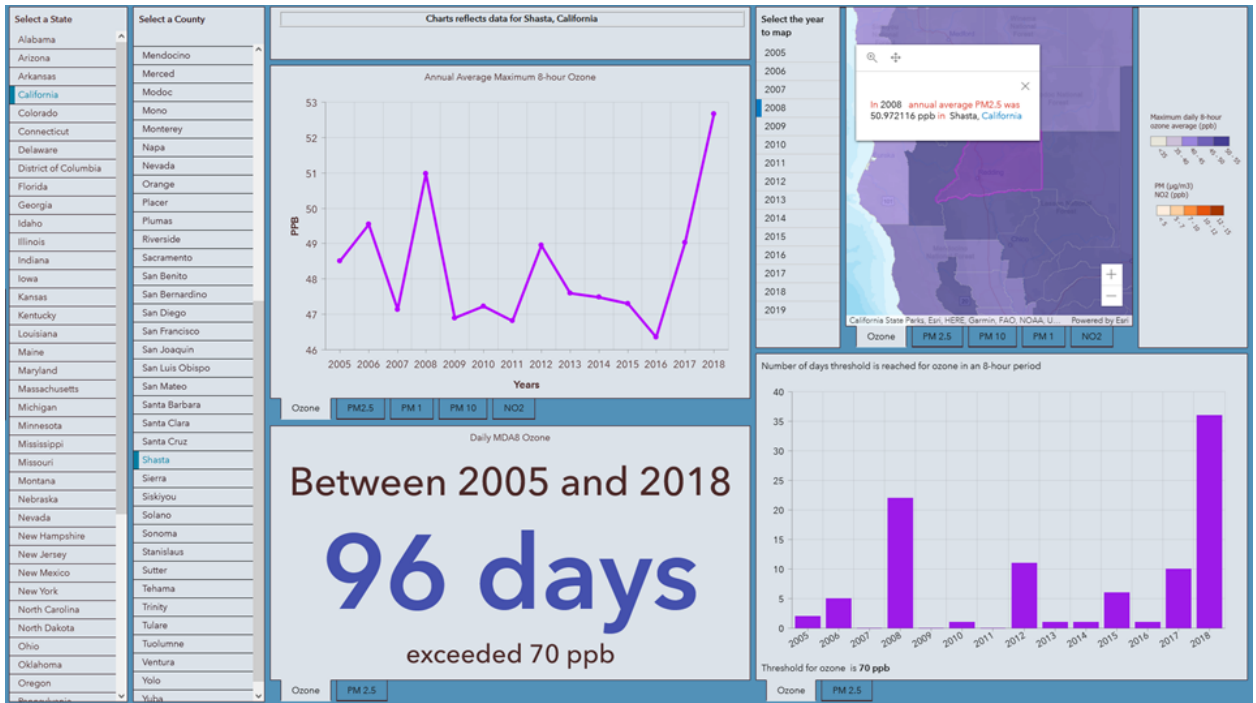
625

626 **Figure 10:** Spatial distribution of positive (blue colors), negative trends (red colors) in 24-hour

627 avg. PM_{2.5} (right panel) at different statistically significant levels (p-values) using monthly median

628 time series (top to bottom). Plots on the right show differences in trend values [CMAQ-AQS].

629



630

631 **Figure 11:** Dashboard reflecting Ozone concentrations for Shasta, CA.

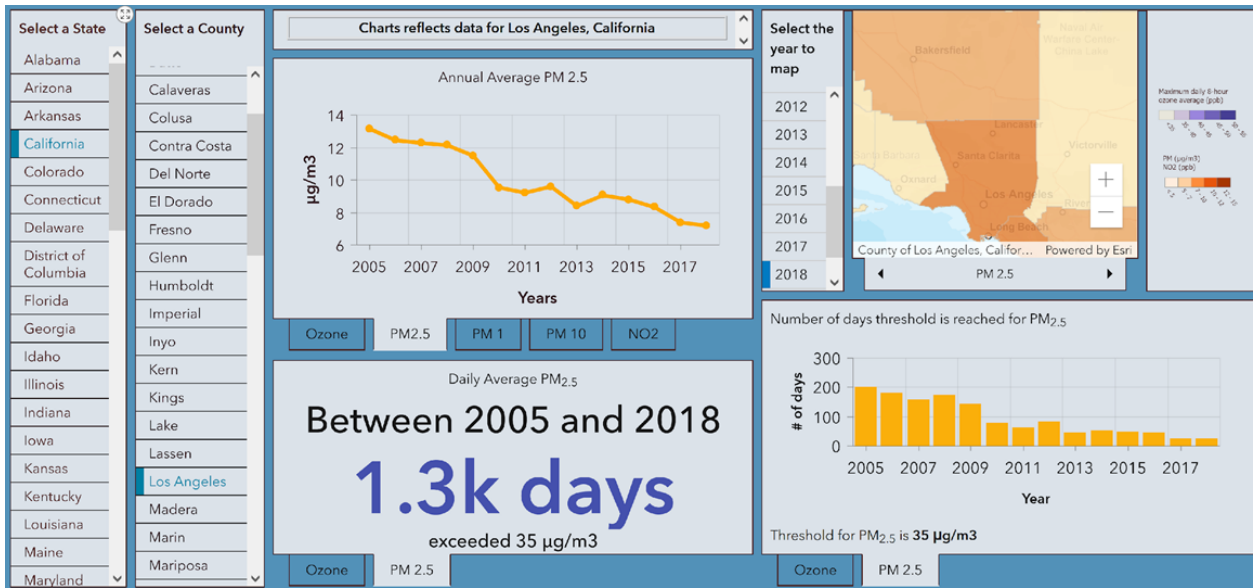
632

633

634

635

636



637

638 **Figure 12:** PM_{2.5} concentrations for Los Angeles, CA.

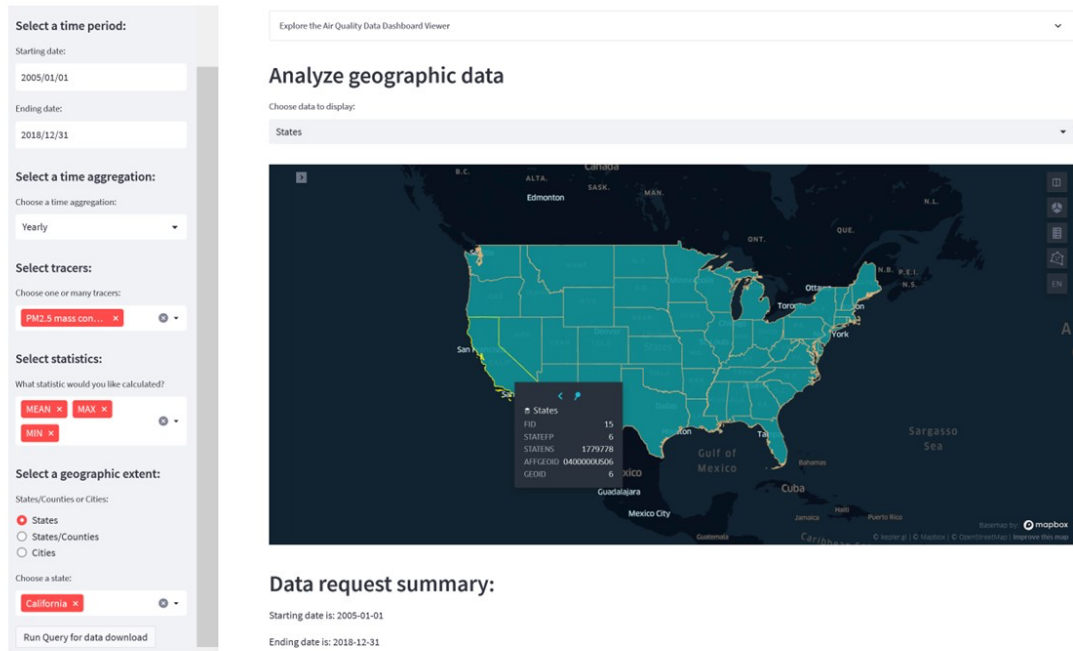
639

640

641

642

643



644

645 **Figure 13:** Streamlit Air Quality App to easily download and summarize data in a CSV format.

646

647

648

649 **9. Appendices**

650 **A1: Forward and Adjoint operators for MOPITT CO assimilation**

651 MOPITT retrieved profile consists of 10 levels, including a surface level followed by 100 hPa
 652 thick layers from 900 hPa to 100 hPa. The CMAQ vertical profile of CO cannot be compared with
 653 MOPITT CO directly and needs to be convolved with the MOPITT a priori profile and averaging
 654 kernel. Following (Barré et al., 2015; Gaubert et al., 2016), the CMAQ profile that can be
 655 compared directly to MOPITT can be written as:

$$656 CO_{ret}^{CMAQ} = 10^{(AK^{MOPITT} \log_{10}(CO^{CMAQ}) + (I - AK^{MOPITT}) \log_{10}(CO_{apr}^{MOPITT}))} \quad (1)$$

657
 658 CO_{ret}^{CMAQ} is the CMAQ CO profile convolved with MOPITT a priori averaging kernel (AK^{MOPITT})
 659 and a priori profile (CO_{apr}^{MOPITT}) that can be compared directly to the MOPITT retrieved CO profile.

660 CO^{CMAQ} is the 10-layer CMAQ profile mapped to the MOPITT pressure grid. A
 661 \log_{10} transformation is necessary because the averaging kernel matrix for retrievals is obtained
 662 with CO parameters in $\log_{10}(CO)$. Differentiation of equation (1) will yield the sensitivity of
 663 CO_{ret}^{CMAQ} with respect to CO^{CMAQ} , which represents the adjoint of the forward operator. For the
 664 purpose of derivation, let $CO_{ret}^{CMAQ} = y$; $CO^{CMAQ} = x$; $AK^{MOPITT} = A$; and $(I -$
 665 $AK^{MOPITT}) \log_{10}(CO_{apr}^{MOPITT}) = C$ then equation (1) can be written as:

$$666 y = 10^{(A \log_{10}(x) + C)} \quad (2)$$

667 Applying the differentiation rule $\frac{d[a^u]}{dx} = \ln(a) \cdot a^u \cdot \frac{du}{dx}$; we can differentiate equation (2) as:

$$668 \frac{dy}{dx} = \ln(10) \cdot 10^{(A \log_{10}(x) + C)} \cdot \frac{d}{dx} (A \log_{10}(x) + C) \quad (3)$$

669 Since A and C do not depend on CMAQ simulations, they are constants and thus their
 670 differentiation is zero. Since $\frac{d}{dx} (\log_{10}(x)) = \frac{1}{x \ln(10)}$, equation (3) simplifies to

671 $\frac{dy}{dx} = 10^{(A \log_{10}(x) + C)} \cdot A \cdot \frac{1}{x} = A \cdot \frac{y}{x}$ (4)

672 Substituting the values of $y, x, A,$ and C in equation (4), the changes in CO vertical profile in the
 673 MOPITT space can be related to changes in CO vertical profile in CMAQ as follows:

674 $dCO_{ret}^{CMAQ} = AK^{MOPITT} \cdot \frac{CO_{ret}^{CMAQ}}{CO^{CMAQ}} dCO^{CMAQ}$ (5)

675 By writing equation (5) in matrix form and then transposing the forward operator matrix, we can
 676 write the adjoint of the forward operator as a recursive matrix equation:

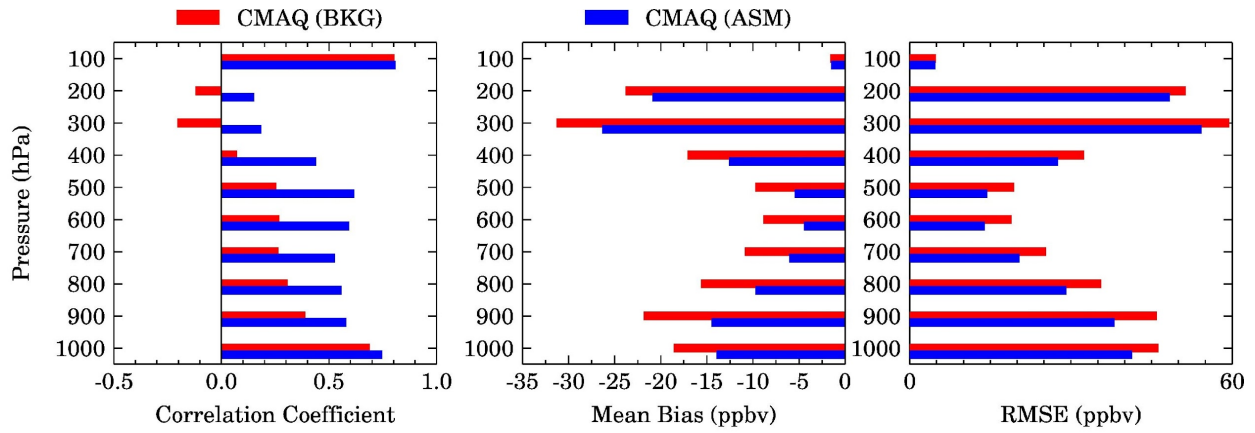
677 $dCO^{CMAQ} = dCO_{ret}^{CMAQ} + AK^{MOPITT} \cdot \frac{CO_{ret}^{CMAQ}}{CO^{CMAQ}} dCO_{ret}^{CMAQ}$ (6)

678

679

680 **A2: Additional Figures**

681



682

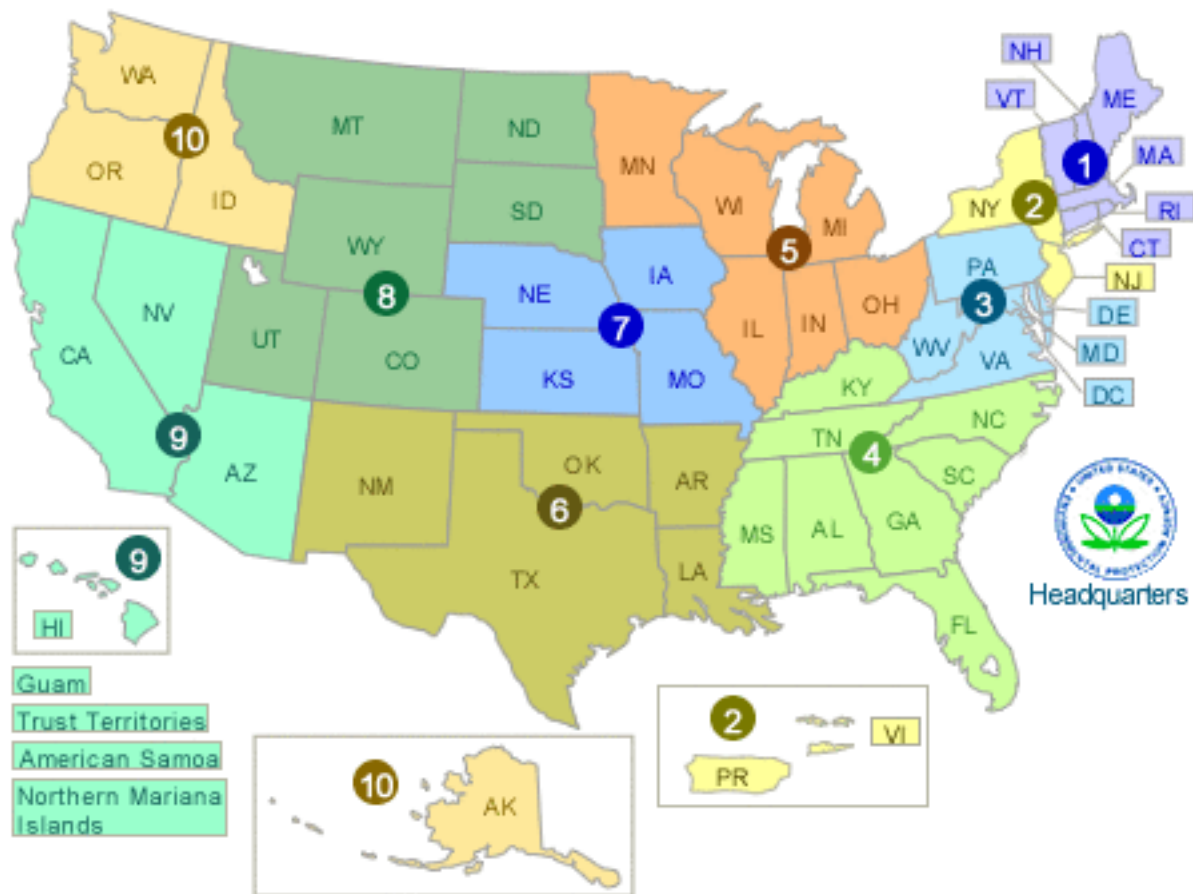
683 **Figure A2.1:** Correlation coefficient, Mean bias, and Root Mean Squared Error (RMSE)

684 between CMAQ and MOPITT CO profiles at ten MOPITT retrievals pressure levels for the

685 CMAQ experiments with (ASM) and without (BKG) assimilation of the MOPITT CO profiles

686 during July 2018. These statistics are based on 118552 data points at each level.

687



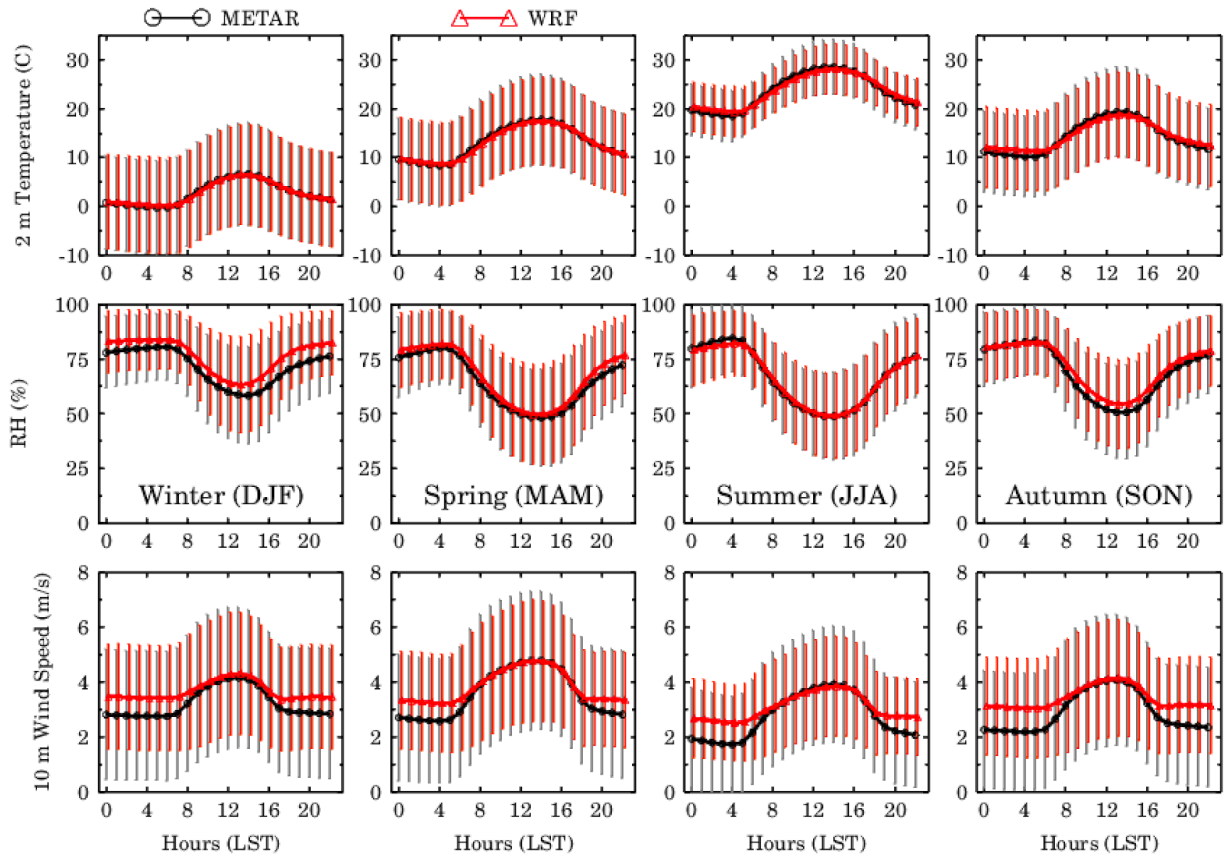
688

689 **Figure A2.2:** Map showing the EPA regions over which model evaluation has been performed.

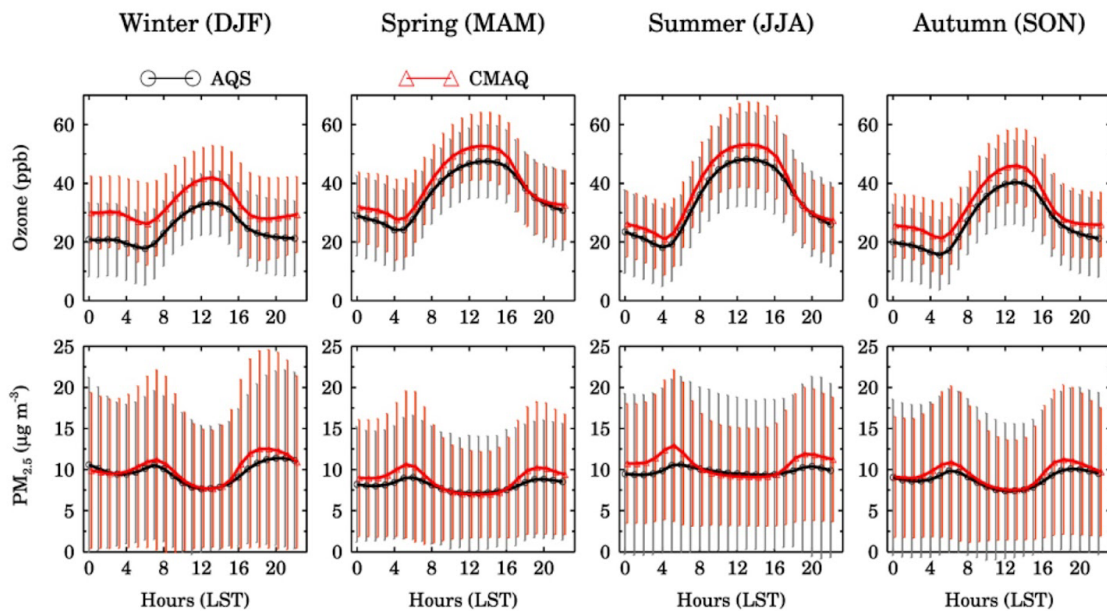
690 The map is reproduced from <https://www.epa.gov/aboutepa/visiting-regional-office>. Our

691 evaluation does not include Puerto Rico in Region 2, Hawaiian Islands in Region 9, and Alaska

692 in Region 10.



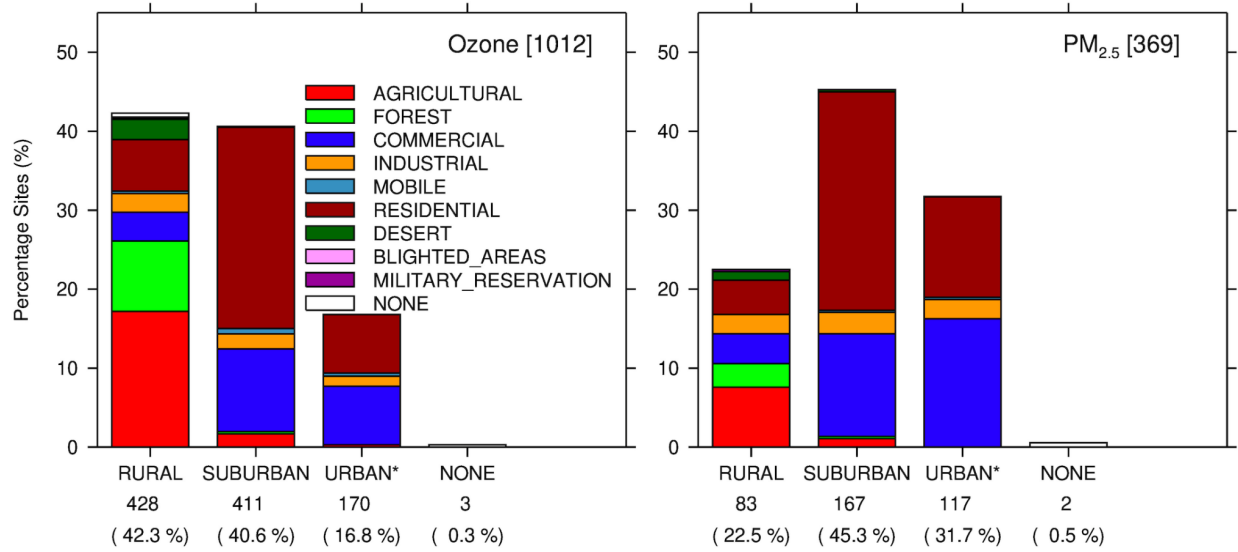
693
 694 **Figure A2.3:** Seasonal mean diurnal variations in 2 m Temperature (Top panel), relative
 695 humidity (middle panel) and 10 m wind speed (bottom panel) from METAR observations and
 696 WRF model.



697

698 **Figure A2.4:** Average diurnal profile of ozone (top panel) and PM_{2.5} (bottom panel) over all
 699 AQS sites in CONUS.

700



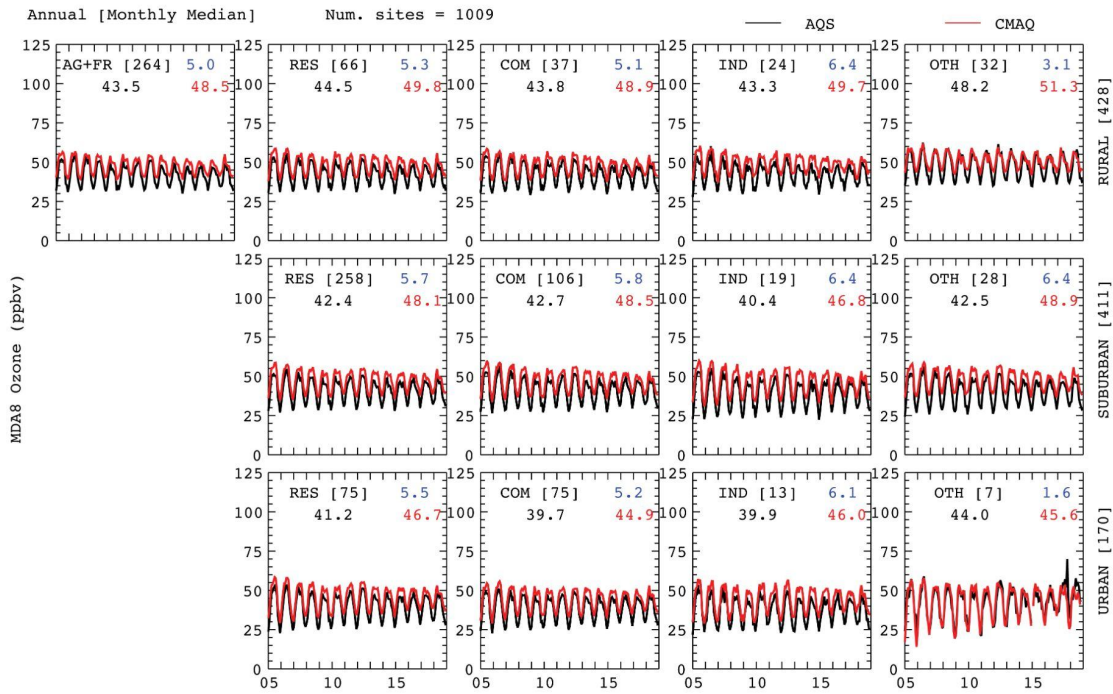
701

702 **Figure A2.5:** The stacked histogram shows the number of sites in each location setting (different
 703 bars) and land use type (different colors) for MDA8 ozone (left) and 24-hr avg. PM_{2.5} (right).

704

705

706

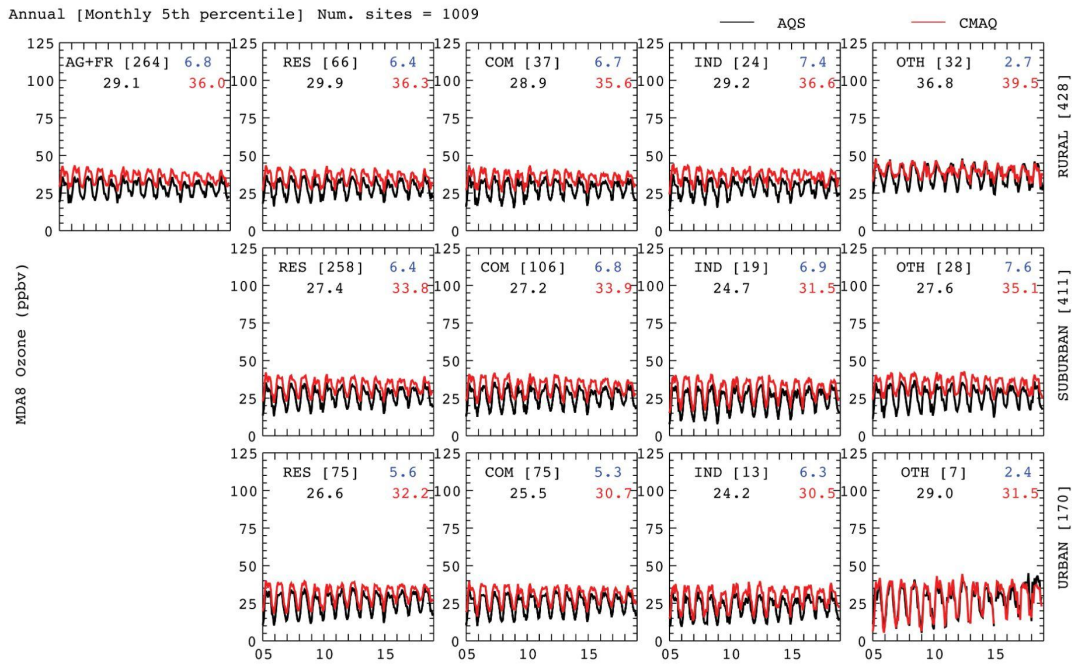


707

708 **Figure A2.6:** The Annual mean (derived from monthly median values) time series of MDA8
 709 Ozone using AQS data (black) and CMAQ (red) over different location type (top to bottom) and
 710 land-use type (left to right) during 2005-2018. The number of sites for each scenario are presented
 711 in brackets. The blue color represents the mean bias.

712

713

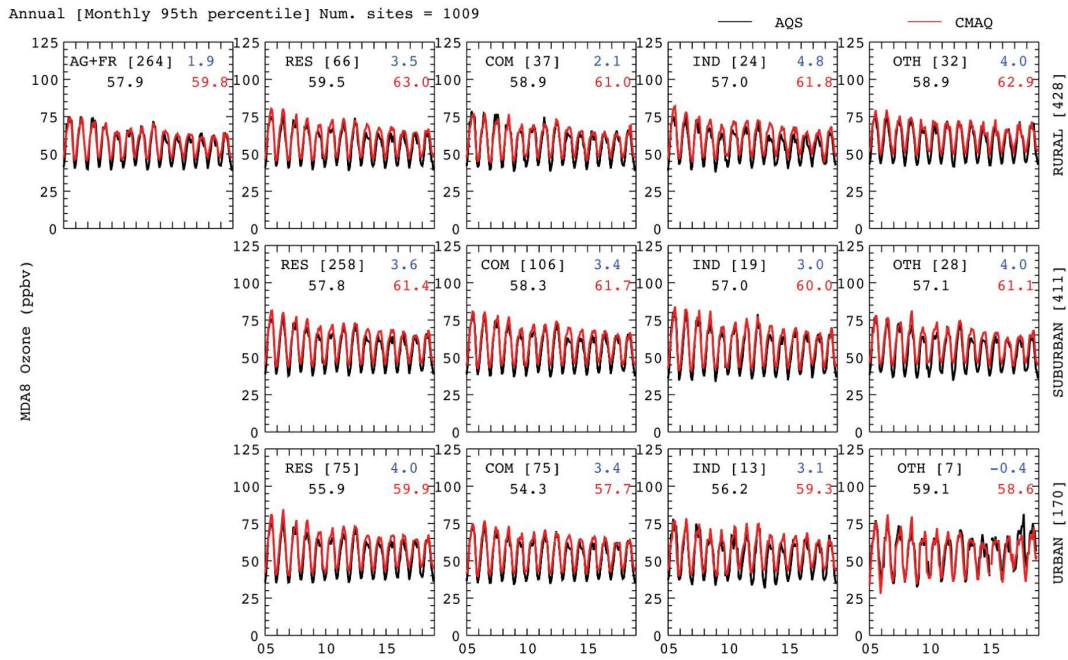


714

715 **Figure A2.7:** Same as Figure A2.6 but time series is derived from monthly 5th percentile values

716

717

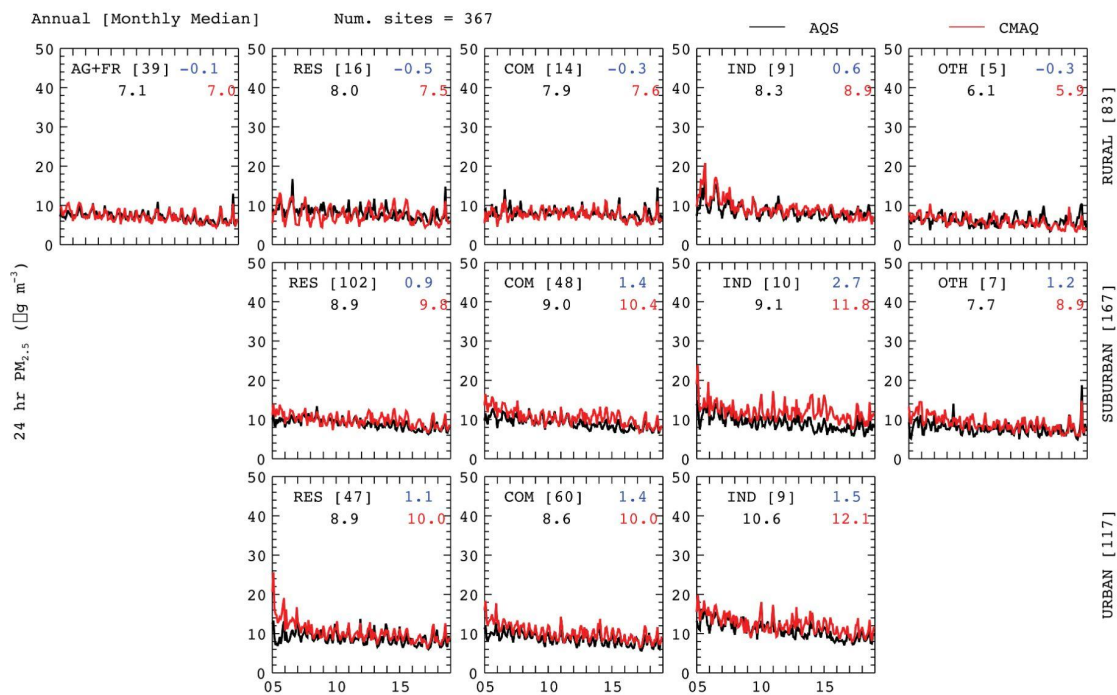


718

719 **Figure A2.8:** Same as Figure A2.6 but time series is derived from monthly 95th percentile values.

720

721

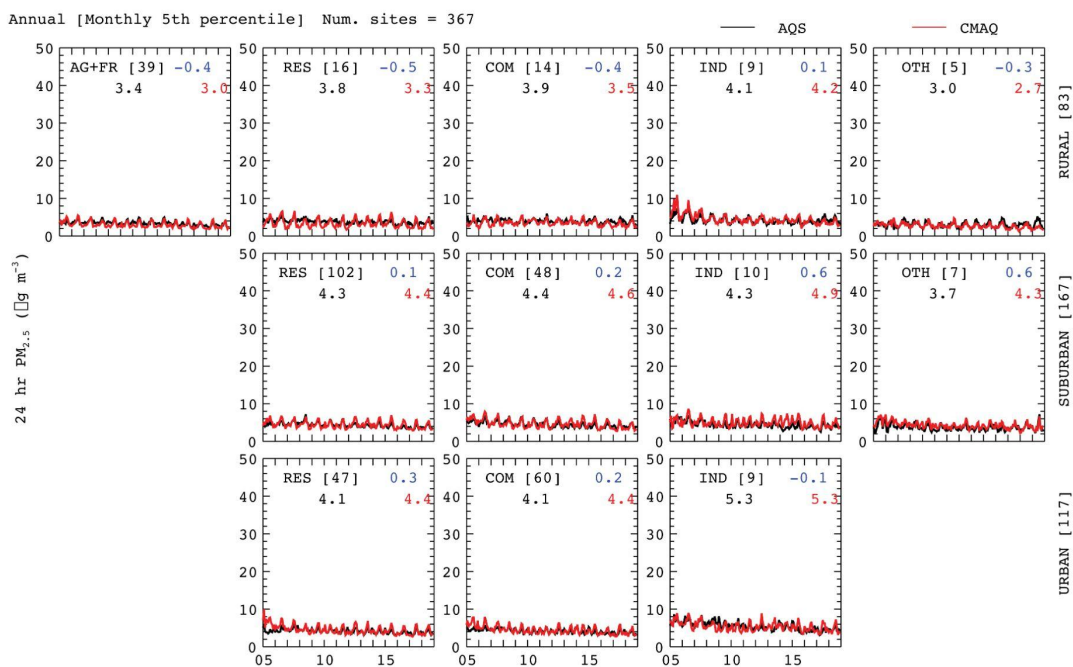


722

723 **Figure A2.9:** The Annual mean (derived from monthly values) time series of 24-hour avg. $PM_{2.5}$
 724 using AQS data (black) and CMAQ (red) over different location types (top to bottom) and land-
 725 use type (left to right) during 2005-18. The number of sites for each scenario are presented in
 726 brackets. The blue color represents the mean bias.

727

728

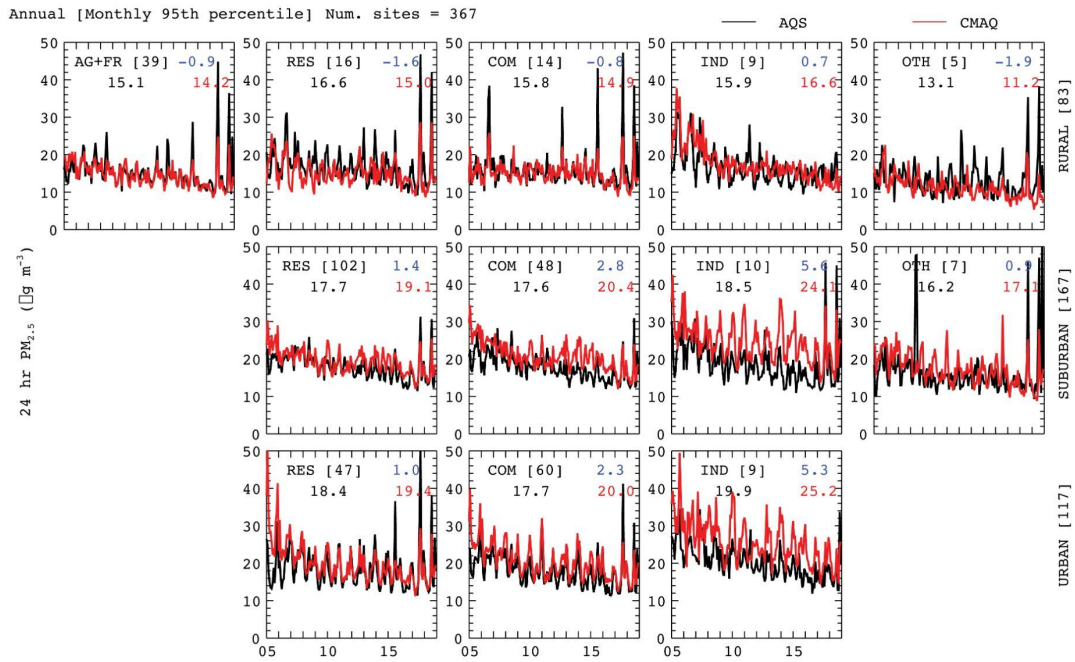


729

730 **Figure A2.10:** Same as Figure A2.9 but time series is derived from monthly 5th percentile values.

731

732



733

734 **Figure A2.11:** Same as Figure A2.9 but time series is derived from monthly 95th percentile values.

735

736

737

738

739

740

741

742

743

744

745

746

747 **A3: Additional Tables**

748 **Table A3.1:** Key physics and chemical schemes used in the WRF-CMAQ configuration.

| Physics | Setup-1 (standard simulation used for assimilation) | Setup-2 (sensitivity simulation used to generate background error) |
|-------------------------------------|--|---|
| Long-wave radiation | RRTMG | RRTM Longwave |
| Short-wave radiation | RRTMG | Goddard Shortwave |
| Microphysics | Morrison double-moment | Thomson |
| Cumulus | Kain–Fritsch version 2 | Grell 3-D ensemble |
| Land surface model | Pleim–Xiu LSM | Unified Noah LSM |
| Surface Layer | Pleim–Xiu surface layer | MYNN |
| PBL | ACM2 | MYNN level 2.5 |
| Gas-phase chemistry | CB06 | CB06 |
| Aerosol chemistry | AERO7 | AERO7 |
| Anthropogenic and fire emissions | EPA NEI | EPA NEI perturbed by factors* derived from uncertainty analysis of multiple emission datasets |
| Biogenic emission | Online CMAQ BEIS | Offline MEGAN |

749

750 **Table A3.2:** Annual anthropogenic emissions for nine species over CONUS during 2005-2018.

| Emissions (Tg/yr) | HTAP v2 [2010] | EDGAR v4.3.2 [2010] | MACCity [2005-16] | CAMsv4.2 [2005-16] | NEI+ [2014] | Min-Max Ratio |
|------------------------------|---------------------------|------------------------------------|------------------------------|-------------------------------|------------------------|--------------------------|
| CO | 56.20 | 56.77 | 46.02 ± 6.39 | 56.49 ± 6.46 | 45.69 | 1.24 |
| NH₃ | 4.42 | 5.14 | 4.44 ± 0.14 | 5.12 ± 0.07 | 3.25 | 1.58 |
| NO_x | 11.07 | 10.93 | 10.40 ± 1.00 | 10.46 ± 0.96 | 12.03 | 1.16 |
| SO₂ | 13.10 | 12.52 | 10.87 ± 2.44 | 11.48 ± 1.90 | 4.46 | 2.94 |
| CH₂O | 0.12 | 0.20 | 0.17 ± 0.02 | 0.26 ± 0.02 | 0.16 | 2.17 |
| NMVOC | 15.61 | 14.57 | 6.58 ± 0.82 | 14.92 ± 0.74 | 12.28 | 2.37 |
| OC | 0.61 | 0.36 | 0.48 ± 0.08 | 0.36 ± 0.01 | 0.79** | 2.19 |
| BC | 0.34 | 0.20 | 0.28 ± 0.06 | 0.21 ± 0.02 | 0.26** | 1.70 |
| PM_{2.5} | 2.02 | N/A | N/A | N/A | 3.67 | 1.82 |

751 ⁺ Except NEI, all other emissions are simply summed over {20-50 N} & {60-130 W} region

752 ** CONUS PM_{2.5} emissions are 5.15 Tg/yr which has 8% BC (or EC) and 28% OC

753 https://www.epa.gov/sites/production/files/2019-08/documents/210pm_rao_508_2.pdf

754

755

756 **Table A3.3:** Annual biomass burning emissions for nine species over the CONUS during 2005-
 757 2018.

| Emissions (Tg/yr) | Top-Down emissions | | Bottom-up emissions | | | Min-Max Ratio |
|------------------------------|---------------------------|-----------------|----------------------------|-----------------|------------|--------------------------|
| | QFED | GFASv1.3 | FINNv1.5 | GFEDv4.1 | NEI | |
| CO | 12.90 ± 2.59 | 8.99 ± 2.40 | 10.93 ± 2.21 | 5.41 ± 1.12 | 16.95 | 3.13 |
| NH₃ | 0.56 ± 0.11 | 0.12 ± 0.03 | 0.18 ± 0.04 | 0.07 ± 0.02 | 0.27 | 8.00 |
| NO_x | 0.56 ± 0.11 | 0.20 ± 0.06 | 0.47 ± 0.10 | 0.18 ± 0.04 | 0.25 | 3.11 |
| SO₂ | 0.32 ± 0.07 | 0.07 ± 0.02 | 0.09 ± 0.02 | 0.04 ± 0.01 | 0.13 | 8.00 |
| CH₂O | 0.16 ± 0.03 | 0.15 ± 0.04 | 0.15 ± 0.03 | 0.10 ± 0.02 | 0.22 | 2.20 |
| tVOC | 0.53 ± 0.11 | 1.05 ± 0.28 | 1.86 ± 0.40 | 1.06 ± 0.22 | 3.92 | 7.40 |
| OC | 2.99 ± 0.63 | 0.60 ± 0.17 | 0.66 ± 0.13 | 0.34 ± 0.09 | 0.45 | 8.79 |
| BC | 0.24 ± 0.05 | 0.05 ± 0.02 | 0.06 ± 0.01 | 0.03 ± 0.01 | 0.15 | 8.00 |
| PM_{2.5} | 4.37 ± 0.92 | 0.90 ± 0.24 | N/A | 0.61 ± 0.14 | 1.48 | 7.16 |

758

759 **10. Author contribution**

760 RK, PB, CH, GGP, SA, HW, and OG conceptualized the study. All the authors contributed to the
761 design of the study. RK, CH, and PB performed all the model simulations including the data
762 assimilation system developments and experiments. PB, CH, RK, and SA contributed to the model
763 evaluation and trend analysis. RK, FL, JB, OG, KS, MC, and SS contributed to the design of the
764 air quality dashboard and Streamlit application. RK prepared the first draft of the paper. All authors
765 contributed to the editing of the manuscript.

766

767 **11. Competing interests**

768 The authors do not have any competing interests. The funding agency had no role in the design of
769 the study, in the collection, analyses, interpretation of data, in the writing of the manuscript,
770 or in the decision to publish the results.

771

772 **12. Financial support**

773 This work is supported by the NASA Atmospheric Composition Modeling and Analysis
774 (ACMAP) Grant # 80NSSC19K0982.

775

776 **13. Acknowledgement**

777 We would like to acknowledge high-performance computing support from Cheyenne (doi:
778 10.5065/D6RX99HX (accessed on 08 June 2023)), provided by NCAR's Computational and
779 Information Systems Laboratory, sponsored by the National Science Foundation. This material is
780 based upon work supported by the NSF National Center for Atmospheric Research, which is a

781 major facility sponsored by the U.S. National Science Foundation under Cooperative Agreement
782 No. 1852977.

783

784 **14. References**

785 Appel, K. W., Bash, J. O., Fahey, K. M., Foley, K. M., Gilliam, R. C., Hogrefe, C., Hutzell, W.

786 T., Kang, D., Mathur, R., Murphy, B. N., Napelenok, S. L., Nolte, C. G., Pleim, J. E.,

787 Pouliot, G. A., Pye, H. O. T., Ran, L., Roselle, S. J., Sarwar, G., Schwede, D. B., Sidi, F.

788 I., Spero, T. L., and Wong, D. C.: The Community Multiscale Air Quality (CMAQ)

789 model versions 5.3 and 5.3.1: system updates and evaluation, *Geoscientific Model*

790 *Development*, 14, 2867–2897, <https://doi.org/10.5194/gmd-14-2867-2021>, 2021.

791 Appel, K. W., Napelenok, S. L., Foley, K. M., Pye, H. O. T., Hogrefe, C., Luecken, D. J., Bash,

792 J. O., Roselle, S. J., Pleim, J. E., Foroutan, H., Hutzell, W. T., Pouliot, G. A., Sarwar, G.,

793 Fahey, K. M., Gantt, B., Gilliam, R. C., Heath, N. K., Kang, D., Mathur, R., Schwede, D.

794 B., Spero, T. L., Wong, D. C., and Young, J. O.: Description and evaluation of the

795 Community Multiscale Air Quality (CMAQ) modeling system version 5.1, *Geoscientific*

796 *Model Development*, 10, 1703–1732, <https://doi.org/10.5194/gmd-10-1703-2017>, 2017.

797 Appel, K. W., Pouliot, G. A., Simon, H., Sarwar, G., Pye, H. O. T., Napelenok, S. L., Akhtar, F.,

798 and Roselle, S. J.: Evaluation of dust and trace metal estimates from the Community

799 Multiscale Air Quality (CMAQ) model version 5.0, *Geoscientific Model Development*, 6,

800 883–899, <https://doi.org/10.5194/gmd-6-883-2013>, 2013.

801 Appel, K. W., Roselle, S. J., Gilliam, R. C., and Pleim, J. E.: Sensitivity of the Community

802 Multiscale Air Quality (CMAQ) model v4.7 results for the eastern United States to MM5

803 and WRF meteorological drivers, *Geoscientific Model Development*, 3, 169–188,

804 <https://doi.org/10.5194/gmd-3-169-2010>, 2010.

805 Atmospheric Environment, Volume 300, 2023, 119693, ISSN 1352-2310,
806 <https://doi.org/10.1016/j.atmosenv.2023.119693>.

807 Barré, J., Gaubert, B., Arellano, A. F. J., Worden, H. M., Edwards, D. P., Deeter, M. N.,
808 Anderson, J. L., Raeder, K., Collins, N., Tilmes, S., Francis, G., Clerbaux, C., Emmons,
809 L. K., Pfister, G. G., Coheur, P.-F., and Hurtmans, D.: Assessing the impacts of
810 assimilating IASI and MOPITT CO retrievals using CESM-CAM-chem and DART,
811 Journal of Geophysical Research: Atmospheres, 120, 10,501-10,529,
812 <https://doi.org/10.1002/2015JD023467>, 2015.

813 Bloomer, B. J., Vinnikov, K. Y., and Dickerson, R. R.: Changes in seasonal and diurnal cycles of
814 ozone and temperature in the eastern U.S., Atmospheric Environment, 44, 2543–2551,
815 <https://doi.org/10.1016/j.atmosenv.2010.04.031>, 2010.

816 Burke M., Childs M. L., de la Cuesta B., Qiu M., Li J., Gould C. F., Heft-Neal S., Wara M.: The
817 contribution of wildfire to PM_{2.5} trends in the USA. Nature 622, 761–766.
818 <https://doi.org/10.1038/s41586-023-06522-6>, 2023.

819 Butler, T. J., Vermeylen, F. M., Rury, M., Likens, G. E., Lee, B., Bowker, G. E., and McCluney,
820 L.: Response of ozone and nitrate to stationary source NO_x emission reductions in the
821 eastern USA, Atmospheric Environment, 45, 1084–1094,
822 <https://doi.org/10.1016/j.atmosenv.2010.11.040>, 2011.

823 Chang, K.-L., Petropavlovskikh, I., Cooper, O. R., Schultz, M. G., and Wang, T.: Regional trend
824 analysis of surface ozone observations from monitoring networks in eastern North
825 America, Europe and East Asia, Elementa: Science of the Anthropocene, 5, 50,
826 <https://doi.org/10.1525/elementa.243>, 2017.

827 Cooper, O. R., Gao, R.-S., Tarasick, D., Leblanc, T., and Sweeney, C.: Long-term ozone trends

828 at rural ozone monitoring sites across the United States, 1990–2010, *Journal of*
829 *Geophysical Research: Atmospheres*, 117, <https://doi.org/10.1029/2012JD018261>, 2012.

830 Deeter, M. N., Edwards, D. P., Francis, G. L., Gille, J. C., Mao, D., Martínez-Alonso, S.,
831 Worden, H. M., Ziskin, D., and Andreae, M. O.: Radiance-based retrieval bias mitigation
832 for the MOPITT instrument: the version 8 product, *Atmospheric Measurement*
833 *Techniques*, 12, 4561–4580, <https://doi.org/10.5194/amt-12-4561-2019>, 2019.

834 Dennison, P. E., Brewer, S. C., Arnold, J. D., and Moritz, M. A.: Large wildfire trends in the
835 western United States, 1984–2011, *Geophysical Research Letters*, 41, 2928–2933,
836 <https://doi.org/10.1002/2014GL059576>, 2014.

837 Di, Q., Wang, Y., Zanobetti, A., Wang, Y., Koutrakis, P., Choirat, C., Dominici, F., and
838 Schwartz, J. D.: Air Pollution and Mortality in the Medicare Population, *New England*
839 *Journal of Medicine*, 376, 2513–2522, <https://doi.org/10.1056/NEJMoa1702747>, 2017.

840 Fahey, K. M., Carlton, A. G., Pye, H. O. T., Baek, J., Hutzell, W. T., Stanier, C. O., Baker, K. R.,
841 Appel, K. W., Jaoui, M., and Offenberg, J. H.: A framework for expanding aqueous
842 chemistry in the Community Multiscale Air Quality (CMAQ) model version 5.1,
843 *Geoscientific Model Development*, 10, 1587–1605, [https://doi.org/10.5194/gmd-10-](https://doi.org/10.5194/gmd-10-1587-2017)
844 [1587-2017](https://doi.org/10.5194/gmd-10-1587-2017), 2017.

845 Fiore, A. M., Jacob, D. J., Bey, I., Yantosca, R. M., Field, B. D., Fusco, A. C., and Wilkinson, J.
846 G.: Background ozone over the United States in summer: Origin, trend, and contribution
847 to pollution episodes, *Journal of Geophysical Research: Atmospheres*, 107, ACH 11-1-
848 ACH 11-25, <https://doi.org/10.1029/2001JD000982>, 2002.

849 Fleming, Z. L., Doherty, R. M., Schneidemesser, E. von, Malley, C. S., Cooper, O. R., Pinto, J.
850 P., Colette, A., Xu, X., Simpson, D., Schultz, M. G., Lefohn, A. S., Hamad, S., Moolla,

851 R., Solberg, S., and Feng, Z.: Tropospheric Ozone Assessment Report: Present-day ozone
852 distribution and trends relevant to human health, *Elem Sci Anth*, 6, 12,
853 <https://doi.org/10.1525/elementa.273>, 2018.

854 Gan, C.-M., Pleim, J., Mathur, R., Hogrefe, C., Long, C. N., Xing, J., Wong, D., Gilliam, R., and
855 Wei, C.: Assessment of long-term WRF–CMAQ simulations for understanding direct
856 aerosol effects on radiation “brightening” in the United States, *Atmospheric Chemistry
857 and Physics*, 15, 12193–12209, <https://doi.org/10.5194/acp-15-12193-2015>, 2015.

858 Gaubert, B., Arellano, A. F., Barré, J., Worden, H. M., Emmons, L. K., Tilmes, S., Buchholz, R.
859 R., Vitt, F., Raeder, K., Collins, N., Anderson, J. L., Wiedinmyer, C., Alonso, S. M.,
860 Edwards, D. P., Andreae, M. O., Hannigan, J. W., Petri, C., Strong, K., and Jones, N.:
861 Toward a chemical reanalysis in a coupled chemistry-climate model: An evaluation of
862 MOPITT CO assimilation and its impact on tropospheric composition, *Journal of
863 Geophysical Research: Atmospheres*, 121, 7310–7343,
864 <https://doi.org/10.1002/2016JD024863>, 2016.

865 Gaubert, B., Worden, H. M., Arellano, A. F. J., Emmons, L. K., Tilmes, S., Barré, J., Alonso, S.
866 M., Vitt, F., Anderson, J. L., Alkemade, F., Houweling, S., and Edwards, D. P.: Chemical
867 Feedback From Decreasing Carbon Monoxide Emissions, *Geophys. Res. Lett.*, 44, 9985–
868 9995, <https://doi.org/10.1002/2017GL074987>, 2017.

869 Gettelman, A., Mills, M. J., Kinnison, D. E., Garcia, R. R., Smith, A. K., Marsh, D. R., Tilmes,
870 S., Vitt, F., Bardeen, C. G., McInerny, J., Liu, H.-L., Solomon, S. C., Polvani, L. M.,
871 Emmons, L. K., Lamarque, J.-F., Richter, J. H., Glanville, A. S., Bacmeister, J. T.,
872 Phillips, A. S., Neale, R. B., Simpson, I. R., DuVivier, A. K., Hodzic, A., and Randel, W.
873 J.: The Whole Atmosphere Community Climate Model Version 6 (WACCM6), *Journal*

874 of Geophysical Research: Atmospheres, 124, 12380–12403,
875 <https://doi.org/10.1029/2019JD030943>, 2019.

876 Hand, J. L., Schichtel, B. A., Malm, W. C., and Frank, N. H.: Spatial and Temporal Trends in
877 PM_{2.5} Organic and Elemental Carbon across the United States, *Advances in Meteorology*,
878 2013, e367674, <https://doi.org/10.1155/2013/367674>, 2013.

879 He, H., Liang, X.-Z., Sun, C., Tao, Z., and Tong, D. Q.: The long-term trend and production
880 sensitivity change in the US ozone pollution from observations and model simulations,
881 *Atmos. Chem. Phys.*, 20, 3191–3208, <https://doi.org/10.5194/acp-20-3191-2020>, 2020.

882 Im, U., Brandt, J., Geels, C., Hansen, K. M., Christensen, J. H., Andersen, M. S., Solazzo, E.,
883 Kioutsioukis, I., Alyuz, U., Balzarini, A., Baro, R., Bellasio, R., Bianconi, R., Bieser, J.,
884 Colette, A., Curci, G., Farrow, A., Flemming, J., Fraser, A., Jimenez-Guerrero, P.,
885 Kitwiroon, N., Liang, C.-K., Nopmongcol, U., Pirovano, G., Pozzoli, L., Prank, M., Rose,
886 R., Sokhi, R., Tuccella, P., Unal, A., Vivanco, M. G., West, J., Yarwood, G., Hogrefe, C.,
887 and Galmarini, S.: Assessment and economic valuation of air pollution impacts on human
888 health over Europe and the United States as calculated by a multi-model ensemble in the
889 framework of AQMEII3, *Atmospheric Chemistry and Physics*, 18, 5967–5989,
890 <https://doi.org/10.5194/acp-18-5967-2018>, 2018.

891 Inness, A., Ades, M., Agustí-Panareda, A., Barré, J., Benedictow, A., Blechschmidt, A.-M.,
892 Dominguez, J. J., Engelen, R., Eskes, H., Flemming, J., Huijnen, V., Jones, L., Kipling,
893 Z., Massart, S., Parrington, M., Peuch, V.-H., Razinger, M., Remy, S., Schulz, M., and
894 Suttie, M.: The CAMS reanalysis of atmospheric composition, *Atmospheric Chem.*
895 *Phys.*, 19, 3515–3556, <https://doi.org/10.5194/acp-19-3515-2019>, 2019.

896 Jaffe, D. and Ray, J.: Increase in surface ozone at rural sites in the western US, *Atmospheric*

897 Environment, 41, 5452–5463, <https://doi.org/10.1016/j.atmosenv.2007.02.034>, 2007.

898 Jaffe, D., Price, H., Parrish, D., Goldstein, A., and Harris, J.: Increasing background ozone
899 during spring on the west coast of North America, *Geophysical Research Letters*, 30,
900 <https://doi.org/10.1029/2003GL017024>, 2003.

901 Kong, L., Tang, X., Zhu, J., Wang, Z., Li, J., Wu, H., Wu, Q., Chen, H., Zhu, L., Wang, W., Liu,
902 B., Wang, Q., Chen, D., Pan, Y., Song, T., Li, F., Zheng, H., Jia, G., Lu, M., Wu, L., and
903 Carmichael, G. R.: A 6-year-long (2013–2018) high-resolution air quality reanalysis
904 dataset in China based on the assimilation of surface observations from CNEMC, *Earth
905 Syst. Sci. Data*, 13, 529–570, <https://doi.org/10.5194/essd-13-529-2021>, 2021.

906 Koumoutsaris, S. and Bey, I.: Can a global model reproduce observed trends in summertime
907 surface ozone levels?, *Atmospheric Chemistry and Physics*, 12, 6983–6998,
908 <https://doi.org/10.5194/acp-12-6983-2012>, 2012.

909 Kumar, Rajesh, and He, C. (2023). CONUS air quality reanalysis dataset (2005-2018). Version
910 1.0. UCAR/NCAR - GDEX. <https://doi.org/10.5065/cfya-4g50>. Accessed 15 May 2024.

911 Kumar, R., Monache, L. D., Bresch, J., Saide, P. E., Tang, Y., Liu, Z., Silva, A. M. da,
912 Alessandrini, S., Pfister, G., Edwards, D., Lee, P., and Djalalova, I.: Toward Improving
913 Short-Term Predictions of Fine Particulate Matter Over the United States Via
914 Assimilation of Satellite Aerosol Optical Depth Retrievals, *Journal of Geophysical
915 Research: Atmospheres*, 124, 2753–2773, <https://doi.org/10.1029/2018JD029009>, 2019.

916 Lin, M., Horowitz, L. W., Payton, R., Fiore, A. M., and Tonnesen, G.: US surface ozone trends
917 and extremes from 1980 to 2014: quantifying the roles of rising Asian emissions,
918 domestic controls, wildfires, and climate, *Atmos. Chem. Phys.*, 17, 2943–2970,
919 <https://doi.org/10.5194/acp-17-2943-2017>, 2017.

920 Liu, Z., Liu, Q., Lin, H.-C., Schwartz, C. S., Lee, Y.-H., and Wang, T.: Three-dimensional
921 variational assimilation of MODIS aerosol optical depth: Implementation and application
922 to a dust storm over East Asia, *Journal of Geophysical Research: Atmospheres*, 116,
923 <https://doi.org/10.1029/2011JD016159>, 2011.

924 Malm, W. C. and Hand, J. L.: An examination of the physical and optical properties of aerosols
925 collected in the IMPROVE program, *Atmospheric Environment*, 41, 3407–3427,
926 <https://doi.org/10.1016/j.atmosenv.2006.12.012>, 2007.

927 Marsh, D. R., Mills, M. J., Kinnison, D. E., Lamarque, J.-F., Calvo, N., and Polvani, L. M.:
928 Climate Change from 1850 to 2005 Simulated in CESM1(WACCM), *J. Climate*, 26,
929 7372–7391, <https://doi.org/10.1175/JCLI-D-12-00558.1>, 2013.

930 McClure, C. D. and Jaffe, D.: US particulate matter air quality improves except in wildfire-prone
931 areas, *PNAS*, 115, 7901–7906, <https://doi.org/10.1073/pnas.1804353115>, 2018.

932 Miyazaki, K., Bowman, K., Sekiya, T., Eskes, H., Boersma, F., Worden, H., Livesey, N., Payne,
933 V. H., Sudo, K., Kanaya, Y., Takigawa, M., and Ogochi, K.: Updated tropospheric
934 chemistry reanalysis and emission estimates, TCR-2, for 2005–2018, *Earth Syst. Sci.*
935 *Data*, 12, 2223–2259, <https://doi.org/10.5194/essd-12-2223-2020>, 2020.

936 Nolte, C. G., Appel, K. W., Kelly, J. T., Bhave, P. V., Fahey, K. M., Collett, J. L. J., Zhang, L.,
937 and Young, J. O.: Evaluation of the Community Multiscale Air Quality (CMAQ) model
938 v5.0 against size-resolved measurements of inorganic particle composition across sites in
939 North America, *Geoscientific Model Development*, 8, 2877–2892,
940 <https://doi.org/10.5194/gmd-8-2877-2015>, 2015.

941 Orozco, D., Reeves, U., and Levine, N.: Polluted Parks: How Air Pollution and Climate Change
942 Continue to Harm America’s National Parks., National Parks Conservation Association

943 (NPCA). Washington, DC., 2024.

944 Pagowski, M., Liu, Z., Grell, G. A., Hu, M., Lin, H.-C., and Schwartz, C. S.: Implementation of
945 aerosol assimilation in Gridpoint Statistical Interpolation (v. 3.2) and WRF-Chem (v.
946 3.4.1), *Geoscientific Model Development*, 7, 1621–1627, [https://doi.org/10.5194/gmd-7-](https://doi.org/10.5194/gmd-7-1621-2014)
947 1621-2014, 2014.

948 Parrish, D. D., Dunlea, E. J., Atlas, E. L., Schauffler, S., Donnelly, S., Stroud, V., Goldstein, A.
949 H., Millet, D. B., McKay, M., Jaffe, D., Price, H. U., Hess, P. G., Flocke, F., and Roberts,
950 J. M.: Changes in the photochemical environment of the temperate North Pacific
951 troposphere in response to increased Asian emissions, *Journal of Geophysical Research:*
952 *Atmospheres*, 109, <https://doi.org/10.1029/2004JD004978>, 2004.

953 Parrish, D. D., Millet, D. B., and Goldstein, A. H.: Increasing ozone in marine boundary layer
954 inflow at the west coasts of North America and Europe, *Atmospheric Chemistry and*
955 *Physics*, 9, 1303–1323, <https://doi.org/10.5194/acp-9-1303-2009>, 2009.

956 Pozzoli, L., Janssens-Maenhout, G., Diehl, T., Bey, I., Schultz, M. G., Feichter, J., Vignati, E.,
957 and Dentener, F.: Re-analysis of tropospheric sulfate aerosol and ozone for the period
958 1980–2005 using the aerosol-chemistry-climate model ECHAM5-HAMMOZ,
959 *Atmospheric Chemistry and Physics*, 11, 9563–9594, [https://doi.org/10.5194/acp-11-](https://doi.org/10.5194/acp-11-9563-2011)
960 9563-2011, 2011.

961 Remer, L. A., Kaufman, Y. J., Tanré, D., Mattoo, S., Chu, D. A., Martins, J. V., Li, R.-R.,
962 Ichoku, C., Levy, R. C., Kleidman, R. G., Eck, T. F., Vermote, E., and Holben, B. N.:
963 The MODIS Aerosol Algorithm, Products, and Validation, *J. Atmos. Sci.*, 62, 947–973,
964 <https://doi.org/10.1175/JAS3385.1>, 2005.

965 Saide, P. E., Carmichael, G. R., Liu, Z., Schwartz, C. S., Lin, H. C., da Silva, A. M., and Hyer,

966 E.: Aerosol optical depth assimilation for a size-resolved sectional model: impacts of
967 observationally constrained, multi-wavelength and fine mode retrievals on regional scale
968 analyses and forecasts, *Atmospheric Chemistry and Physics*, 13, 10425–10444,
969 <https://doi.org/10.5194/acp-13-10425-2013>, 2013.

970 Seyedali Mousavinezhad, Masoud Ghahremanloo, Yunsoo Choi, Arman Pouyaei, Nima
971 Khorshidian, Bavand Sadeghi, Surface ozone trends and related mortality across the
972 climate regions of the contiguous United States during the most recent climate period,
973 1991–2020,

974 Simon, H., Reff, A., Wells, B., Xing, J., and Frank, N.: Ozone Trends Across the United States
975 over a Period of Decreasing NO_x and VOC Emissions, *Environ. Sci. Technol.*, 49, 186–
976 195, <https://doi.org/10.1021/es504514z>, 2015.

977 Strode, S. A., Rodriguez, J. M., Logan, J. A., Cooper, O. R., Witte, J. C., Lamsal, L. N., Damon,
978 M., Van Aartsen, B., Steenrod, S. D., and Strahan, S. E.: Trends and variability in surface
979 ozone over the United States, *Journal of Geophysical Research: Atmospheres*, 120, 9020–
980 9042, <https://doi.org/10.1002/2014JD022784>, 2015.

981 WHO: Billions of people still breathe unhealthy air: new WHO data:
982 [https://www.who.int/news/item/04-04-2022-billions-of-people-still-breathe-unhealthy-](https://www.who.int/news/item/04-04-2022-billions-of-people-still-breathe-unhealthy-air-new-who-data)
983 [air-new-who-data](https://www.who.int/news/item/04-04-2022-billions-of-people-still-breathe-unhealthy-air-new-who-data), last access: 12 May 2024, 2023.

984 WHO: <https://www.who.int/westernpacific/health-topics/air-pollution> , last access: 12 May
985 2024, 2020.

986 Wiedinmyer, C., Kimura, Y., McDonald-Buller, E. C., Emmons, L. K., Buchholz, R. R., Tang,
987 W., Seto, K., Joseph, M. B., Barsanti, K. C., Carlton, A. G., and Yokelson, R.: The Fire
988 Inventory from NCAR version 2.5: an updated global fire emissions model for climate

989 and chemistry applications, EGU sphere, 1–45, [https://doi.org/10.5194/egusphere-2023-](https://doi.org/10.5194/egusphere-2023-124)
990 124, 2023.

991 Xie, Y., Lin, M., & Horowitz, L. W.: Summer PM_{2.5} pollution extremes caused by wildfires
992 over the western United States during 2017–2018. *Geophysical Research Letters*, 47,
993 e2020GL089429. <https://doi.org/10.1029/2020GL089429>, 2020.

994 Xing, J., Mathur, R., Pleim, J., Hogrefe, C., Gan, C.-M., Wong, D. C., Wei, C., Gilliam, R., and
995 Pouliot, G.: Observations and modeling of air quality trends over 1990–2010 across the
996 Northern Hemisphere: China, the United States and Europe, *Atmospheric Chemistry and*
997 *Physics*, 15, 2723–2747, <https://doi.org/10.5194/acp-15-2723-2015>, 2015.

998 Zhang, Y., West, J. J., Mathur, R., Xing, J., Hogrefe, C., Roselle, S. J., Bash, J. O., Pleim, J. E.,
999 Gan, C.-M., and Wong, D. C.: Long-term trends in the ambient PM_{2.5}- and O₃-related
1000 mortality burdens in the United States under emission reductions from 1990 to 2010,
1001 *Atmospheric Chemistry and Physics*, 18, 15003–15016, [https://doi.org/10.5194/acp-18-](https://doi.org/10.5194/acp-18-15003-2018)
1002 15003-2018, 2018.